

# Multiparameter optimization for ground-state cooling of a mechanical mode using quantum dots

Neelesh Kumar Vij <sup>1</sup>, Harish S. Adsule <sup>2</sup>, Meenakshi Khosla,<sup>3</sup> and Shilpi Gupta <sup>4,5,\*</sup>

<sup>1</sup>*Department of Electrical and Computer Engineering and Institute for Research in Electronics and Applied Physics, University of Maryland, College Park, Maryland 20742, USA*

<sup>2</sup>*Department of Physics, Indian Institute of Technology Kanpur, Kanpur 208016, Uttar Pradesh, India*

<sup>3</sup>*Department of Brain and Cognitive Sciences, Massachusetts Institute of Technology, Cambridge, Massachusetts 02139, USA*

<sup>4</sup>*Department of Electrical Engineering, Indian Institute of Technology Kanpur, Kanpur 208016, Uttar Pradesh, India*

<sup>5</sup>*Centre for Lasers and Photonics, Indian Institute of Technology Kanpur, Kanpur 208016, Uttar Pradesh, India*



(Received 2 August 2023; revised 2 February 2024; accepted 9 February 2024; published 7 March 2024)

Cooling a mechanical mode to its motional ground state opens up avenues for both scientific and technological advancements in the field of quantum metrology and information processing. We propose a multiparameter optimization scheme for ground-state cooling of a mechanical mode using quantum dots. Applying the master-equation approach, we formulate the optimization scheme over a broad range of system parameters including detunings, decay rates, pumping rates, and coupling strengths. We implement the optimization scheme on two major types of semiconductor quantum-dot systems: colloidal and epitaxial quantum dots. These systems span a broad range of mechanical-mode frequencies, coupling rates, and decay rates. Our optimization scheme lowers the steady-state phonon number in all cases by several orders of magnitude and thereby the effective temperature of the mechanical mode by more than an order of magnitude. We also calculate the net cooling rate by estimating the phonon decay rate and show that the optimized system parameters also result in efficient cooling. The proposed optimization scheme can be readily extended to other driven systems coupled to a mechanical mode.

DOI: [10.1103/PhysRevA.109.033510](https://doi.org/10.1103/PhysRevA.109.033510)

## I. INTRODUCTION

Mechanical resonators have been an essential tool for precision metrology for a long time [1]. With the advancements in nanofabrication techniques, efforts are now oriented towards studying the quantum-mechanical aspects of the mechanical resonators [1,2]. Cooling a mechanical resonator mode to its motional ground state is of particular interest because of wide-ranging applications in the fields of quantum metrology [3–7], information processing [8–11], and testing of quantum-classical boundary [12–15].

The coupling of a mechanical resonator mode to a thermal bath, which is usually at a relatively high temperature, results in heating. On the other hand, the coupling of a mechanical resonator mode with a dissipative channel leads to cooling. The competition between these heating and cooling processes determine the extent of cooling of the mechanical resonator mode [16]. Therefore, a general approach to cool the resonator mode to its motional ground state is twofold: (a) Reduce the heating rate by reducing the coupling of the mechanical resonator mode with the thermal bath [17,18] and (b) increase the cooling rate by engineering additional dissipative channels with hybrid quantum-mechanical systems. Various approaches utilizing solid-state systems such as cooling with color centers [19–22], superconducting qubits [23–25], quantum dots [26–29], and optomechanical systems [30–35] have been proposed and studied. To achieve maximum and efficient

cooling of the mechanical mode, system parameters that are within experimental control need to be optimized. Many of these parameters depend on the physical realization of the dissipative channel and have been selectively studied in the literature, for example, detuning between the energy levels of the channel and the input laser [20,23,26,28,32–35], coherent coupling strengths within the channel [19,29–35], and the decay rates of the channel [22,28,29] (detailed comparison in Appendix A). However, simultaneous optimization of multiple system parameters is required to achieve maximum and efficient cooling.

Here we propose a multiparameter optimization scheme to cool a mechanical mode using a semiconductor quantum dot. Semiconductor quantum dots are one of the most mature solid-state systems [36]. They exhibit tunable optical properties and compatibility with complementary metal-oxide semiconductor fabrication technology, allowing for seamless integration into hybrid optomechanical systems at micro- and nanoscales [37,38]. We formulate an optimization problem over various detunings, decay rates, pumping rates, and coupling strengths of the system using the master-equation formalism. We particularly show cooling of a mechanical mode by coupling to two different types of quantum-dot systems: colloidal and epitaxial quantum dots. We show that multiparameter optimization lowers the steady-state phonon number of the mechanical mode by several orders of magnitude. We also calculate the effective temperature of the mechanical mode at steady state and show a reduction in temperature by factors of approximately 14 and 32 for the two quantum-dot systems. We further calculate

\*Corresponding author: [ShilpiG@iitk.ac.in](mailto:ShilpiG@iitk.ac.in)

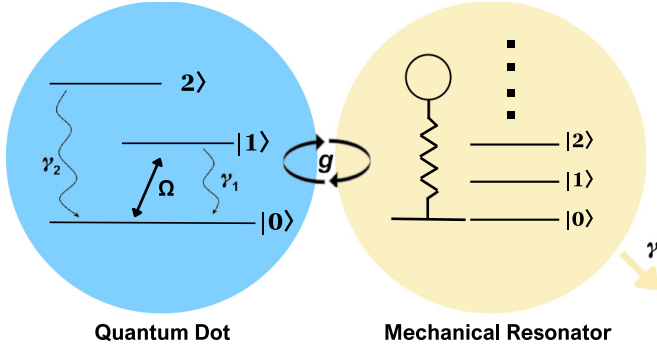


FIG. 1. Schematic representing a quantum dot coupled to a mode of a mechanical resonator.

the effective phonon decay rate and show that the optimized system parameters simultaneously result in maximum and efficient cooling.

## II. DESCRIPTION OF THE SYSTEM

### A. Hamiltonian and master equation

The two widely studied quantum-dot systems, i.e., a colloidal quantum dot and an epitaxial quantum dot strongly coupled to an optical cavity, are routinely modeled as three-level systems [39–42]. The three levels in the model for a colloidal quantum dot represent the ground state, the dark exciton, and the bright exciton [39,42]. Similarly, the three levels in the model for an epitaxial quantum dot strongly coupled to an optical cavity represent the ground state, the lower polariton, and the upper polariton [40,41]. The energy differences between the bright and the dark exciton of a colloidal quantum dot and between the upper polariton and the lower polariton in the strongly coupled epitaxial quantum-dot–cavity system are in the regime of mechanical-mode energies. Therefore, we model a quantum dot as a three-level system comprising the ground state  $|0\rangle$ , the first excited state  $|1\rangle$ , and the second excited state  $|2\rangle$  (Fig. 1). The phonon mode of the mechanical resonator is coupled to the two excited states of the three-level quantum-dot system with strength  $g$ . We also include a coherent pump of strength  $\Omega$  at frequency  $\omega_p$  between the states  $|0\rangle$  and  $|1\rangle$ . The system Hamiltonian can thus be written as ( $\hbar = 1$ )

$$\begin{aligned} \mathbf{H}_{\text{system}} = & \omega_1 \sigma_{11} + \omega_2 \sigma_{22} + \omega_m b^\dagger b + g(\sigma_{12} b^\dagger + \sigma_{21} b) \\ & + \Omega(\sigma_{01} e^{i\omega_p t} + \sigma_{10} e^{-i\omega_p t}), \end{aligned} \quad (1)$$

where  $\omega_1$  and  $\omega_2$  are frequencies of the states  $|1\rangle$  and  $|2\rangle$ , respectively, and  $\omega_m$  is the frequency of the phonon mode. The operator  $\sigma_{ij} = |i\rangle\langle j|$  represents the population operator when  $i = j$  and the dipole operator when  $i \neq j$ . The annihilation (creation) operator for the phonon mode is  $b$  ( $b^\dagger$ ). We set the energy of the ground state of the three-level system to zero. To remove the time-dependent terms, we move to a suitable rotated frame and obtain the rotated Hamiltonian (see

derivation in Appendix B)

$$\begin{aligned} \mathbf{H}_{\text{rotated}} = & \Delta_1 \sigma_{11} + (\Delta_1 + \Delta_2) \sigma_{22} + \Omega(\sigma_{01} + \sigma_{10}) \\ & + g(\sigma_{12} b^\dagger + \sigma_{21} b), \end{aligned} \quad (2)$$

where  $\Delta_1 = \omega_1 - \omega_p$  and  $\Delta_2 = \omega_2 - \omega_1 - \omega_m$ . To analyze the complete dynamics of the system, we use the Lindblad master equation for the combined density operator  $\rho$  under the Born-Markov approximation:

$$\begin{aligned} \frac{d\rho}{dt} = & i[\rho, \mathbf{H}_{\text{rotated}}] + \gamma_1 \mathcal{L}[\sigma_{01}]\rho + \gamma_2 \mathcal{L}[\sigma_{02}]\rho \\ & + \gamma(n_{\text{th}} + 1) \mathcal{L}[b]\rho + \gamma n_{\text{th}} \mathcal{L}[b^\dagger]\rho. \end{aligned} \quad (3)$$

Here  $\mathcal{L}[\mathcal{O}]\rho = \mathcal{O}\rho\mathcal{O}^\dagger - (\mathcal{O}^\dagger\mathcal{O}\rho + \rho\mathcal{O}^\dagger\mathcal{O})/2$ ,  $\gamma_1$  and  $\gamma_2$  are the decay rates of  $|1\rangle$  and  $|2\rangle$ , respectively,  $\gamma$  is the decay rate of the phonon mode, and  $n_{\text{th}} = 1/(e^{\beta\omega_m} - 1)$  is the phonon number in thermal equilibrium at inverse temperature  $\beta = 1/k_B T$  and frequency  $\omega_m$ . The second and third terms in Eq. (3) represent the decay of the first and second excited states to the ground state, respectively, by coupling to the optical bath. The last two terms in Eq. (3) account for the coupling of the mechanical mode with the bath held at a constant temperature  $T$  (Fig. 1).

Our cooling scheme, which utilizes a quantum dot as the dissipative channel to lower the average phonon number of a mechanical mode, can be understood as follows. A coherent pump drives the population between the states  $|0\rangle$  and  $|1\rangle$ . The population in the state  $|1\rangle$  transitions to the state  $|2\rangle$  by absorbing a near-resonant phonon from the coupled mechanical mode. The population in the state  $|2\rangle$  then decays to the ground state via the emission of a photon, leading to an overall decrease in the number of phonons in the mechanical mode. We will use Eq. (2) in the following section to set up the optimization problem to achieve the minimum phonon number in the mechanical mode in the steady state.

### B. Deriving the optimization problem

We write the Heisenberg operator equations (Appendix C) for the expectation value of the phonon-number operator  $b^\dagger b$  and the population operator of the second excited state  $\sigma_{22}$ :

$$\begin{aligned} \frac{d\langle b^\dagger b \rangle}{dt} = & ig\langle \sigma_{21} b - \sigma_{12} b^\dagger \rangle + \gamma(n_{\text{th}} - \langle b^\dagger b \rangle), \\ \frac{d\langle \sigma_{22} \rangle}{dt} = & ig\langle \sigma_{12} b^\dagger - \sigma_{21} b \rangle - \gamma_2 \langle \sigma_{22} \rangle. \end{aligned} \quad (4)$$

Solving the above equations in steady state gives

$$\langle b^\dagger b \rangle_{\text{ss}} = n_{\text{th}} - \frac{\gamma_2}{\gamma} \langle \sigma_{22} \rangle_{\text{ss}}, \quad (5)$$

where the subscript denotes the expectation values calculated in the steady state. Equation (5) reveals the inherent optimization problem present in the combined system. To minimize the steady-state phonon number in the mechanical mode, we need to maximize the term  $\gamma_2 \langle \sigma_{22} \rangle_{\text{ss}}$ . However, as we increase  $\gamma_2$ , the steady-state population of the state  $|2\rangle$ , represented by  $\langle \sigma_{22} \rangle_{\text{ss}}$ , decreases and vice versa. Thus, an optimal value of  $\gamma_2$  exists, which leads to the minimum phonon number. The optimization also depends on the other parameters of the system (decay rates, detunings, coupling strength, and

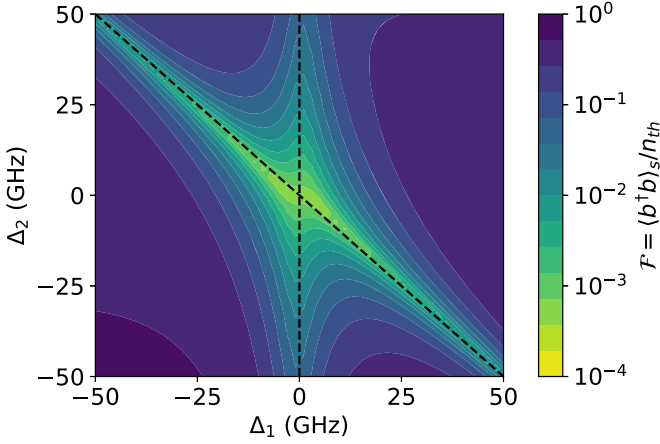


FIG. 2. Variation of  $\mathcal{F} = \langle b^\dagger b \rangle_{ss} / n_{th}$  with detunings  $\Delta_1$  and  $\Delta_2$ . The other parameters are  $g = 5$  GHz,  $\omega_2 - \omega_1 = 120.9$  GHz,  $\gamma_2 = \Omega = g/2$ ,  $\gamma_1 = 10^{-1}g$ ,  $\gamma = 10^{-4}g$ , an initial temperature of 50 K, and the cutoff for the mechanical resonator Fock state basis  $N = 10$ .

pumping strength) that come into play via the expression of  $\langle \sigma_{22} \rangle_{ss}$ . Next we analyze the role of each of these parameters in minimizing the steady-state phonon number.

Depending on the platform in which a mechanical mode coupled to a quantum dot is realized, the coupling strengths and the decay rates can range from megahertz to gigahertz [26,39]. For this section we set  $g = 5$  GHz,  $\omega_2 - \omega_1 = 120.9$  GHz, and an initial temperature of the combined system to 50 K, as a generic set of parameters. We also define a figure of merit for cooling of the mechanical mode as  $\mathcal{F} = \langle b^\dagger b \rangle_{ss} / n_{th}$ , which needs to be minimized [22].

### 1. Effect of detunings

First we analyze the effect of the detunings  $\Delta_1$  and  $\Delta_2$  on the figure of merit  $\mathcal{F}$ . For this calculation, we set  $\gamma_2 = \Omega = g/2$ ,  $\gamma_1 = 10^{-1}g$ , and  $\gamma = 10^{-4}g$ . Using Eqs. (2), (4), and (5) and the quantum toolbox QUTIP [43], we calculate variation of  $\mathcal{F}$  with detunings  $\Delta_1$  and  $\Delta_2$  (Fig. 2). The cutoff for the Fock state basis of the mechanical resonator mode in the quantum toolbox simulations is set to  $N = 10$  (Appendix D). We vary  $\Delta_1$  and  $\Delta_2$  by varying the pump frequency  $\omega_p$  and the phonon mode frequency  $\omega_m$ , respectively. As expected, for far-off-resonant interactions,  $\mathcal{F} \approx 1$ , implying negligible cooling. Minimization of the figure of merit is achieved along the dashed lines  $\Delta_1 = 0$ , which represents resonance between the pump and the  $|0\rangle - |1\rangle$  transition, and  $\Delta_2 = -\Delta_1$ , which represents resonance between the phonon mode and the  $|1\rangle - |2\rangle$  transition assisted by the pump. Global minimization of  $\mathcal{F}$  happens when both  $\Delta_1 = 0$  and  $\Delta_2 = 0$ . However, we note that even when the phonon mode is off-resonant with the  $|1\rangle - |2\rangle$  transition, i.e.,  $\Delta_2 \neq 0$ , a local minimization of  $\mathcal{F}$  can be achieved by tuning the frequency of the coherent pump such that  $\Delta_1 = -\Delta_2$ . This offers a convenient way to minimize the phonon number in the case of an off-resonant phonon mode.

The optimal values of the detunings  $\Delta_1$  and  $\Delta_2$  are also mandated by the relative strengths of  $g$  and  $\Omega$ . When  $g$  and  $\Omega$  are not of the same order, the minimization of  $\mathcal{F}$  happens for nonzero detuning values (Appendix E 1). Since the pumping

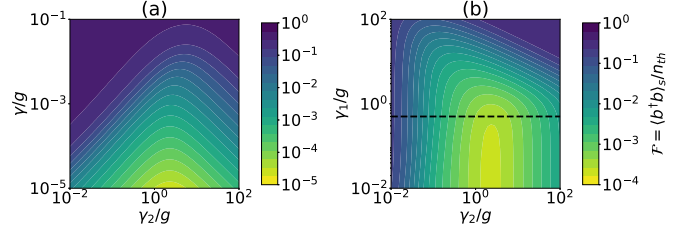


FIG. 3. Variation of  $\mathcal{F}$  with (a) phonon decay rate  $\gamma$  and decay rate of the second excited state  $\gamma_2$  for  $\gamma_1 = 10^{-1}g$  and (b) decay rate of the first excited state  $\gamma_1$  and the second excited state  $\gamma_2$  for  $\gamma = 10^{-4}g$ . The horizontal black dashed line denotes  $\gamma_1 = \Omega$ . The other parameters are  $g = 5$  GHz,  $\Delta_1 = \Delta_2 = 0$ ,  $\omega_2 - \omega_1 = 120.9$  GHz,  $\Omega = g/2$ , an initial temperature of 50 K, and the cutoff for the mechanical resonator Fock state basis  $N = 10$ .

strength  $\Omega$  is a control parameter in experiments, we choose it to be of the same order as  $g$ ,  $\Omega \approx g$ , and set  $\Delta_1 = \Delta_2 = 0$  in further calculations. We note that the optimal values of the detunings are governed by the coherent interactions that are fully accounted for by the system Hamiltonian Eq. (2). Therefore, the optimal values of  $\Delta_1$  and  $\Delta_2$  are invariant to the changes in decay rates.

### 2. Effect of decay rates

Next we analyze the effect of the decay rates on the figure of merit  $\mathcal{F}$ . Figure 3(a) plots the variation of  $\mathcal{F}$  as a function of the phonon decay rate  $\gamma$  and the decay rate of the second excited state  $\gamma_2$ . We set  $\Omega = g/2$  and  $\gamma_1 = 10^{-1}g$  and vary  $\gamma$  and  $\gamma_2$  over a large range of values spanning across four orders of magnitude. We make the following observations.

(i) The  $\mathcal{F}$  decreases as the phonon decay rate  $\gamma$  decreases. A lower  $\gamma$  reduces the interaction of the mechanical mode with the phonon bath, reducing the heating rate of the mechanical mode. For further calculations, we set  $\gamma \ll g$ .

(ii) There exists an optimal decay rate of the second excited state  $\gamma_2$  that minimizes  $\mathcal{F}$ . This observation is consistent with our explanation presented in the beginning of this section using Eq. (5).

Figure 3(b) shows the variation of  $\mathcal{F}$  with  $\gamma_1$  and  $\gamma_2$  for  $\Omega = g/2$  and  $\gamma = 10^{-4}g$ . The black dashed line represents the condition  $\gamma_1 = \Omega$ . Consistent with Fig. 3(a), Fig. 3(b) exhibits the same optimal  $\gamma_2$  when  $\gamma_1 \lesssim \Omega$ , which leads to a globally minimized  $\mathcal{F}$ . When  $\gamma_1 \gtrsim \Omega$ , decoherence sets in between the states  $|0\rangle$  and  $|1\rangle$ , requiring a lower value for optimal  $\gamma_2$  and increasing the minimum achievable value of  $\mathcal{F}$ . When  $\gamma_1 > \Omega$  and  $\gamma_2$  is greater than its optimal value, decoherence dominates and leads to  $\mathcal{F} \approx 1$ , as depicted in the upper right region of the plot. We note that when  $\Omega \neq g$ ,  $\mathcal{F}$  can be minimized either by introducing nonzero detunings (Appendix E 1) or by varying the decay rates (Appendix E 2), both of which lead to an increase in the minimum achievable  $\mathcal{F}$ .

The above discussion gives us a broad set of conditions for the system parameters, which leads to minimization of the figure of merit  $\mathcal{F}$ : (i)  $\Omega \approx g$  with  $\Delta_1 = \Delta_2 = 0$ , (ii)  $\gamma \ll g$ , (iii)  $\gamma_1 \lesssim \Omega$ , and (iv) an optimal value for  $\gamma_2$ . To perform further optimization, we identify the following two regimes of decay rates exemplified by quantum-dot systems:  $\gamma_1 \ll \gamma_2$  and  $\gamma_1 = \gamma_2$ . In the next section, we analytically formulate

the cooling optimization problem for these two regimes and discuss the outcomes for the relevant quantum-dot systems.

### III. COOLING OPTIMIZATION FOR DIFFERENT REGIMES

In this section we derive steady-state analytical models for the two regimes of the decay rates by restricting the excitations of the mechanical resonator phonon mode to one. The approximation is valid because we characterize the mechanical resonator mode in the steady state, which is achieved when the phonon mode is cooled close to the ground state, and thus the probability of higher excitations is negligible. We compare the results of our approximated analytical model with numerical simulations performed for a sufficiently large basis of the phonon mode to ensure numerical stability. Through the comparison, we show that the approximation is indeed valid and later discuss its limitations. Along with the steady-state behavior that is captured by both the analytical model and the numerical simulations, the numerical simulations also capture the time dynamics of the system. Therefore, we calculate the effective phonon decay rate and show that the parameters that minimize the figure of merit also result in a high cooling rate.

#### A. Regime $\gamma_1 \ll \gamma_2$

We derive the equations of motion for the density-matrix elements of the combined system (Appendix F) and solve them under the approximation  $\gamma_1 \ll \gamma_2$  to obtain the expression for the steady-state phonon number [Eq. (F2)]. To set values of the parameters for this regime, we consider a system of a colloidal quantum dot, specifically a cadmium selenide quantum dot coupled to its confined phonon mode via deformation potential. For temperatures less than 20 K, a colloidal quantum dot can be approximated as a three-level system with the first and second excited states  $|1\rangle$  and  $|2\rangle$  being the dark and bright states, respectively [39,42]. The dark state of the colloidal quantum dot has a lifetime of approximately 1 ms and the bright state has a lifetime of approximately 10 ns. Therefore, this colloidal quantum-dot-phonon system exemplifies the regime of  $\gamma_1 \ll \gamma_2$ . To facilitate coherent pumping to the dark state, a two-photon absorption technique can be used [44]. Consistent with the literature [39], for further calculations in this section we set the following values for the system parameters:  $\omega_m = 241.8$  GHz,  $g = 20$  GHz,  $\gamma_1 = 10^{-6}$  GHz,  $\gamma = 10^{-3}$  GHz, an initial temperature of 17 K, and the cutoff for the Fock state  $N = 10$ .

We treat the strength of the coherent pumping  $\Omega$  and the decay rate of the bright state  $\gamma_2$  as the control parameters in this system. The decay rate of the bright state can be altered via Purcell enhancement by coupling to an optical cavity. Purcell factors up to  $10^4$  have been achieved using appropriate cavity geometry [45,46]. Therefore, we plot the figure of merit  $\mathcal{F}$  as a function of  $\Omega$  and  $\gamma_2$  using the expression of  $\langle b^\dagger b \rangle_{ss}$  [Eq. (F2)] in Fig. 4(a). We also numerically calculate  $\mathcal{F}$  by solving the master Eq. (3) using the quantum toolbox with the excitations of the mechanical mode set to  $N = 10$  [Fig. 4(b)]. Both Figs. 4(a) and 4(b) suggest that  $\mathcal{F}$  is minimized for certain values of  $\Omega$  and  $\gamma_2$ , which we next calculate analytically.

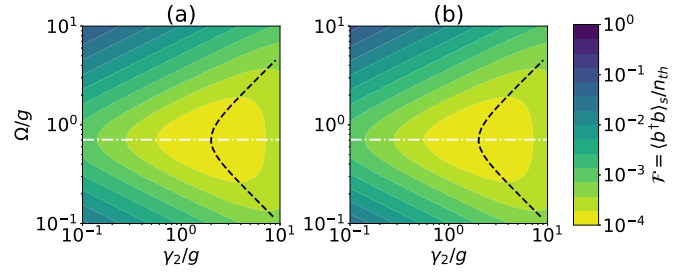


FIG. 4. Regime  $\gamma_1 \ll \gamma_2$ . The variation of  $\mathcal{F}$  with pumping strength  $\Omega$  and decay rate of the second excited state  $\gamma_2$  is found using (a) the approximated analytical model Eq. (F2) and (b) the exact simulation model. The white dot-dashed line and the black dashed curve represent the optimal parameters  $\Omega_o$  and  $\gamma_{2o}$ , respectively, as derived in Eq. (6). The other parameters are  $\omega_m = 241.8$  GHz,  $g = 20$  GHz,  $\gamma_1 = 10^{-6}$  GHz,  $\gamma = 10^{-3}$  GHz, an initial temperature of 17 K, and the cutoff for the mechanical resonator Fock state basis  $N = 10$ .

Since  $\gamma_2 \gg \gamma$ , we neglect the higher-order terms of  $\gamma$  in the expression of  $\langle b^\dagger b \rangle_{ss}$  [Eq. (F2)] and arrive at the following expressions for optimal pumping strength  $\Omega_o$  and optimal decay rate of the second excited state  $\gamma_{2o}$ :

$$\begin{aligned} \Omega_o &= \frac{g}{\sqrt{2}}, \\ \gamma_{2o} &= \sqrt{4\Omega^2 + \frac{g^4}{\Omega^2}}. \end{aligned} \quad (6)$$

We plot  $\Omega_o/g$  as a white dot-dashed line and  $\gamma_{2o}/g$  as a black dashed curve in Fig. 4. We observe that the optimal pumping strength is a function of only the coupling strength, while the optimal decay rate of the second excited state is a function of both the pumping strength and the coupling strength. The optimal pumping strength  $\Omega_o$  depends on only the coupling strength because the decay rate of the first excited state  $\gamma_1$  is negligible compared to the other rates in this system. On the other hand,  $\gamma_{2o}$  depends on  $\Omega$  and  $g$  because the two coherent processes compete with the incoherent process for population transfer to and from the second excited state. We further include the effect of pure dephasing in our numerical simulations by adding Lindblad terms  $\gamma_d \mathcal{L}[\sigma_{11}] \rho$  and  $\gamma_d \mathcal{L}[\sigma_{22}] \rho$  to the master Eq. (3), where  $\gamma_d$  is the pure dephasing rate (Appendix G). We observe that  $\mathcal{F}$  and the optimal values of the pumping strength and the decay rate of the second excited state [Eq. (6)] show negligible variation with the inclusion of pure dephasing rates observed in the literature [39].

The analytical and simulation results are in good agreement, which justifies that the higher-order phonon excitations are sparsely populated and thus can be neglected. The agreement and the proposed model break down when the rate of bulk phonon decaying into the system (equal to  $\gamma n_{th}$ ) is comparable to the coupling strength  $g$ , which happens when either  $n_{th}$ , governed by the initial temperature, or  $\gamma$ , governed by the quality factor of the mechanical mode, is large or both are large. We note that the choice of physical system (quantum dot here) dictates the initial value of  $n_{th}$  and the frequency of the mechanical mode. Our model can be readily extended



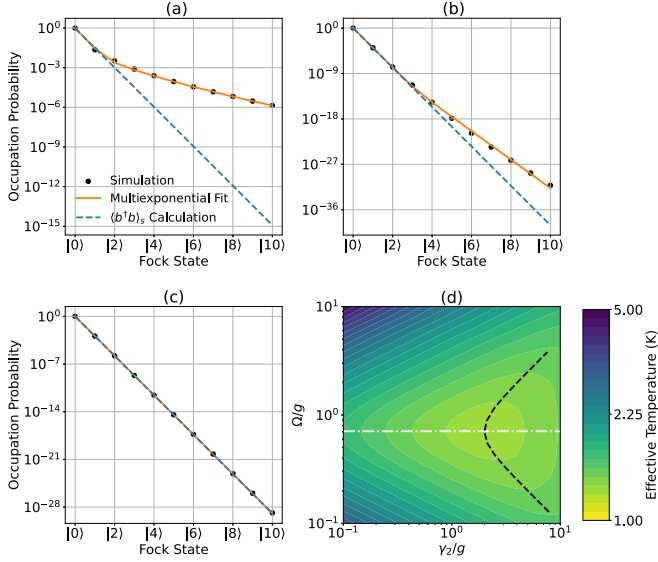


FIG. 5. Regime  $\gamma_1 \ll \gamma_2$ . The distribution of Fock population is plotted as a function of Fock state number for different pumping strengths and decay rates of the second excited state (a)  $\Omega = 0.1g$ ,  $\gamma_2 = 0.1g$ , (b)  $\Omega = 1.0g$ ,  $\gamma_2 = 1.5g$ , and (c)  $\Omega = 10.0g$ ,  $\gamma_2 = 10.0g$ . (d) Variation of effective temperature at steady state with  $\Omega$  and  $\gamma_2$ . The white dot-dashed line and the black dashed curve represent the optimal parameters  $\Omega_o$  and  $\gamma_{2,o}$ , respectively, as derived in Eq. (6). The other parameters are  $\omega_m = 241.8$  GHz,  $g = 20$  GHz,  $\gamma_1 = 10^{-6}$  GHz,  $\gamma = 10^{-3}$  GHz, an initial temperature of 17 K, and the cutoff for the mechanical resonator Fock state basis  $N = 10$ .

to any other physical system obeying the approximations laid out up to now. In order to get a more intuitive estimate of cooling of the mechanical mode, we next calculate an effective temperature of the mechanical mode in the steady state.

**Effective temperature.** For a mechanical mode with frequency  $\omega_m$  and in thermal equilibrium, the density matrix is purely diagonal in the phonon Fock state basis. The diagonal elements of the density matrix of this thermal state represent the Fock state occupation probabilities given by the distribution [47]

$$P_\beta(n) = e^{-n\beta\omega_m} / (1 - e^{-\beta\omega_m}), \quad (7)$$

where  $\beta = 1/k_B T$  is the inverse temperature and  $n$  is the Fock state number. For a thermal state, the probability distribution of Fock state occupation Eq. (7) is a single-exponential function and hence a straight line on a semilogarithmic scale. Also, for a thermal state, the average phonon number is given by  $\langle b^\dagger b \rangle = (e^{\beta\omega_m} - 1)^{-1}$ , which enables calculation of the temperature  $T$  of the mechanical mode in terms of the known  $\langle b^\dagger b \rangle$ .

For our system comprising a colloidal quantum dot coupled to a mechanical mode, we calculate the Fock state occupation probabilities by solving the master Eq. (3) in steady state using the quantum toolbox and plot them on a semilogarithmic scale [black markers in Figs. 5(a)–5(c)]. We observe that the occupation probability plots are not necessarily straight lines, which suggests that the probability distribution for the Fock state occupation in the steady state is not a single-exponential function. Therefore, we fit the calculated occupation

probabilities of Fock states to a multiexponential function given by

$$P(n) = \sum_{i=1}^k c_i P_{\beta_i}(n), \quad (8)$$

where  $c_i$  denotes the weight associated with each exponential term such that  $\sum_{i=1}^k c_i = 1$  and  $P_{\beta_i}(n)$  is given by Eq. (7) [orange curve in Figs. 5(a)–5(c)]. More details on the fitting routine are available in Appendix H.

While performing the multiexponential fits, we observe that a maximum of three different exponential terms is sufficient for a good fit (a maximum mean absolute percentage error of less than 5% across  $\Omega$  and  $\gamma_2$  ranges). Without loss of generality, we assume that the inverse temperatures follow  $\beta_1 > \beta_2 > \beta_3$ . We also observe that the multiexponential distribution is dominated by the exponential term corresponding to  $\beta_1$ , i.e.,  $c_1 \sim 1$  (Appendix H). We note that even though  $c_2$  and  $c_3$  are orders of magnitude smaller than  $c_1$ , they are essential to obtain a good fit on the logarithmic scale, i.e., simply setting  $c_2 = c_3 = 0$  leads to quite a large fitting error. However,  $c_2$  and  $c_3$  have a negligible contribution in statistical averages of measurable quantities of the system, such as the average phonon number. Hence, we assign an effective temperature  $T = 1/\beta_1 k_B$  to the mechanical mode. This effective temperature, obtained from the fitting routine, dominates the initial slope of the Fock state occupation probability function. Using the already calculated steady-state average phonon numbers [Fig. 4(b)], we also backcalculate the temperature of the mechanical mode, assuming it to be in a thermal state [probability distribution shown by blue dashed lines in Figs. 5(a)–5(c)]. This calculated temperature matches extremely well with the effective temperature estimated from the multiexponential fitting. We also observe that the initial slope (i.e., for the first few Fock states) of the multiexponential fit (orange curves) coincides with the slope of the blue dashed line (Fig. 5). This observation further strengthens our assumption of ignoring the higher Fock states in our analytical calculations. We plot the effective temperature as a function of  $\Omega$  and  $\gamma_2$  in Fig. 5(d). At the optimal pumping strength  $\Omega_o$  and optimal decay rate  $\gamma_{2,o}$ , the effective temperature reduces from 17 K to 1.2 K, showing cooling of the mechanical mode by a factor of 14.1.

**Cooling rate.** With the optimization in place, we now estimate the rate of the cooling process by calculating the effective phonon decay rate  $\gamma_{\text{eff}}$ . As the decay of a general mechanical state may involve simultaneous decay of multiple phonon Fock states, it will be a multiexponential decay process. In the literature, the two prominent models used for multiexponential decay processes are the stretched exponential fit [48] and the log-normal fit [49]. Here we employ the stretched exponential fit. Using the Monte Carlo solver in QUTIP (Appendix D), we plot the variation of phonon number with time [Figs. 6(a)–6(f)], using the quantum toolbox, and fit it to a stretched exponential of the form

$$\langle b^\dagger b \rangle(t) = (n_{\text{th}} - \langle b^\dagger b \rangle_{\text{ss}}) e^{-(\gamma_{\text{eff}} t)^\beta} + \langle b^\dagger b \rangle_{\text{ss}}, \quad (9)$$

where  $\langle b^\dagger b \rangle_{\text{ss}}$  is the steady-state phonon number and  $\beta \in (0, 1]$  is the stretch parameter with  $\beta = 1$  representing a single-exponential decay function. The effective phonon

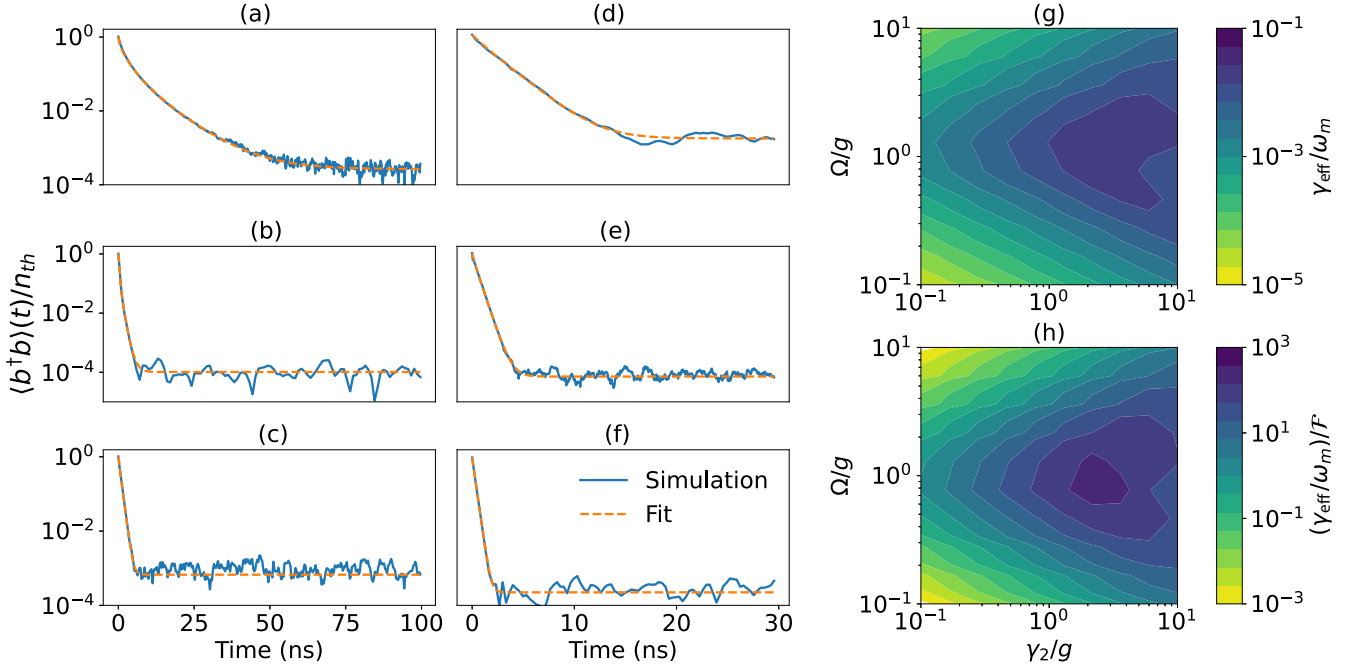


FIG. 6. Regime  $\gamma_1 \ll \gamma_2$ . Time-dependent decay of the average phonon number of the mechanical mode and the corresponding stretched-exponential fit are shown for (a)  $\Omega = 0.25g$  and  $\gamma_2 = 2g$ , (b)  $\Omega = 1g$  and  $\gamma_2 = 2g$ , (c)  $\Omega = 4g$  and  $\gamma_2 = 2g$ , (d)  $\Omega = 2g$  and  $\gamma_2 = 0.25g$ , (e)  $\Omega = 2g$  and  $\gamma_2 = 1g$ , and (f)  $\Omega = 2g$  and  $\gamma_2 = 4g$ . Also shown are (g)  $\gamma_{eff}/\omega_m$  and (h)  $(\gamma_{eff}/\omega_m)/\mathcal{F}$ , over a range of values of  $\Omega$  and  $\gamma_2$ . The other parameters are  $\omega_m = 241.8$  GHz,  $g = 20$  GHz,  $\gamma_1 = 10^{-6}$  GHz,  $\gamma = 10^{-3}$  GHz, an initial temperature of 17 K, the cutoff for the mechanical resonator Fock state basis  $N = 20$ , and 5000 Monte Carlo trajectories.

decay rate depends on the initial condition of the mechanical mode. Here we assume that initially the quantum dot is in the ground state and the mechanical mode is in the thermal state. Repeating the procedure of fitting and extracting the effective phonon decay rate  $\gamma_{eff}$  over a range of values of  $\Omega$  and  $\gamma_2$ , we plot  $\gamma_{eff}/\omega_m$  in Fig. 6(g). From our simulations, we observe that the phonon-decay process is indeed multiexponential because the extracted values of  $\beta$  for the fits are in  $[0.6, 1)$ . The mean absolute percentage error for all the fits is less than 5%. We observe that the same ranges of  $\Omega$  and  $\gamma_2$  maximize  $\gamma_{eff}$  [Fig. 6(g)] and minimize  $\mathcal{F}$  (Fig. 4). To demonstrate this point clearly, we plot the ratio of  $\gamma_{eff}/\omega_m$  to  $\mathcal{F}$  in Fig. 6(h). A large value of this ratio within the optimized ranges of  $\Omega$  and  $\gamma_2$  implies that our optimization process simultaneously ensures maximum and efficient cooling of the mechanical mode.

### B. Regime $\gamma_1 = \gamma_2$

For the  $\gamma_1 = \gamma_2$  regime, we first consider an optical cavity mode strongly coupled to an epitaxial quantum dot, which is modeled as a two-level system (TLS), forming polaritons, which in turn couple to a mode of a mechanical resonator. The Hamiltonian for the system takes the form (Appendix I) [40]

$$\mathbf{H}_{\text{system}} = \omega_1 \sigma_{11} + \omega_2 \sigma_{22} + \omega_m b^\dagger b - \Omega \sin \theta (\sigma_{01} e^{i\omega_p t} + \sigma_{10} e^{-i\omega_p t}) + g \sin \theta \cos \theta (\sigma_{12} b + \sigma_{21} b^\dagger), \quad (10)$$

where  $|1\rangle$  and  $|2\rangle$  are the two polariton states of the cavity-TLS system with frequencies  $\omega_1$  and  $\omega_2$ , respectively,  $|0\rangle$  is the ground state,  $g$  is the coupling strength between the

polariton states and the mechanical resonator mode, and  $\tan(2\theta) = 2G/\Delta$ , with  $G$  and  $\Delta$  the coupling strength and detuning, respectively, between the TLS and the cavity mode. We set the detuning between the TLS and cavity mode to zero ( $\theta = \pi/4$ ), which results in the decay rates  $\gamma_1$  and  $\gamma_2$  of the polariton states being equal [50]. The decay rates  $\gamma_1$  and  $\gamma_2$  are functions of both the quantum dot and the cavity decay rates. We use  $\gamma_2$  to denote both decay rates of this system in further discussion. With this simplification, the Hamiltonian in Eq. (10) is equivalent to the Hamiltonian in Eq. (1). Therefore, the system follows the same optimization rules on pumping strength, detunings, and phonon decay rate as laid out in Sec. II B. For further optimization, we solve the equations of motion for the density-matrix elements of the combined system (Appendix F) to obtain the expression for the steady-state phonon number under the condition  $\gamma_1 = \gamma_2$  [Eq. (F3)].

To set the values of the parameters, we consider an InGaAs quantum dot coupled to a GaAs microdisk cavity. It has been demonstrated that microdisk cavities can support gigahertz-frequency mechanical modes with mechanical quality factors up to  $10^9$  [51], optical quality factors up to  $6 \times 10^6$  [52], and optomechanical coupling strengths in the kilohertz to megahertz range [53]. The coupling strength between the quantum dot and cavity ranges from a few gigahertz to 50 GHz at low temperatures [54,55]. Here we set  $G = 5$  GHz,  $g = 0.002G = 10$  MHz,  $\omega_m = 2G$ ,  $\gamma = \omega_m/Q_m = 10^{-7}$  GHz, and an initial temperature of 2.63 K corresponding to  $n_{th} = 5$ . We choose a small initial temperature to keep computational complexity, associated with a large  $n_{th}$  in quantum toolbox simulations, manageable.

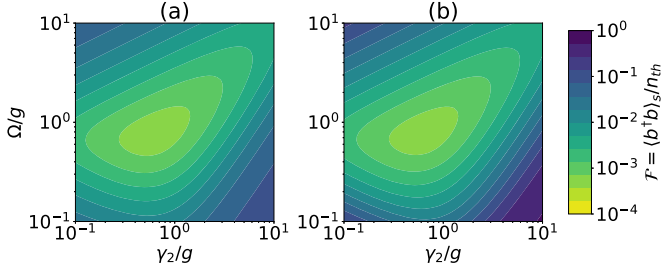


FIG. 7. Regime  $\gamma_1 = \gamma_2$ . The variation of  $\mathcal{F}$  with  $\Omega$  and  $\gamma_2$  is found using (a) the approximated analytical model Eq. (F3) and (b) the exact simulation model. The parameters are  $G = 5$  GHz,  $g = 0.002G = 10$  MHz,  $\omega_m = 2G$ ,  $\gamma = \omega_m/Q_m = 10^{-7}$  GHz, an initial temperature of 2.63 K corresponding to  $n_{th} = 5$ , and the cutoff for the phonon Fock state  $N = 10$ .

We treat the strength of the coherent pumping  $\Omega$  and the decay rate of the polariton states  $\gamma_2 (= \gamma_1)$  as the control parameters. The decay rate  $\gamma_2$  can be enhanced or suppressed by engineering the local density of optical states [41,45,46,56]. Therefore, we plot the figure of merit  $\mathcal{F}$  as a function of  $\Omega$  and  $\gamma_2$  in Fig. 7(a) using the analytically derived expression Eq. (G1) and in Fig. 7(b) by numerically solving the master Eqs. (3) and (10) using the quantum toolbox without the approximations made for the analytical calculations. We observe that the optimal value of  $\Omega$  ( $\gamma_2$ ) is a function of the optomechanical coupling strength and  $\gamma_2$  ( $\Omega$ ). Furthermore, the optimal values of  $\Omega$  and  $\gamma_2$  are of the order of the optomechanical coupling strength  $g$ , as also observed in the colloidal quantum-dot case in Sec. III A, and we again attribute this nature to the competing dynamics of the three rates for population transfer to and from the upper polariton state. Obtaining analytical expressions for optimal  $\Omega$  and  $\gamma_2$  is difficult because of the sheer complexity of the expression of the steady-state phonon number Eq. (F3). However, they can be obtained by fitting appropriate functions to the calculated data.

While deriving the Hamiltonian Eq. (10), we limit the excitations of the optical cavity to one which results in the three-level system for the cavity–quantum-dot system. This assumption can be justified as follows: The coherent pump is resonant with the transition between the ground state  $|0\rangle$  and the lower polariton state  $|1\rangle$  (Appendix I) and the pumping to the higher polariton rungs is off-resonant and therefore suppressed. For the values we consider, more than 99% of the cavity–quantum-dot population is occupied by the polariton states  $\{|0\rangle, |1\rangle, |2\rangle\}$ , thus justifying the assumption.

In the current state-of-the-art microdisk cavities, the decay rate of the cavity mode is of the order of 100 MHz [52] and the decay rate of the quantum dot is of the order of 10 MHz [57]. Therefore, the decay rate of the polariton is dominated by the decay rate of the cavity. For the polariton-coupled mechanical resonator mode case, our optimization scheme requires suppressing the decay rate  $\gamma_2$  because the optomechanical coupling strength is in the megahertz regime. Since the minimum achievable  $\gamma_2$  is currently limited by the cavity decay rate, further improvements in cavity design and fabrication can enable higher optical quality factors and thereby the optimal value of  $\gamma_2$ .

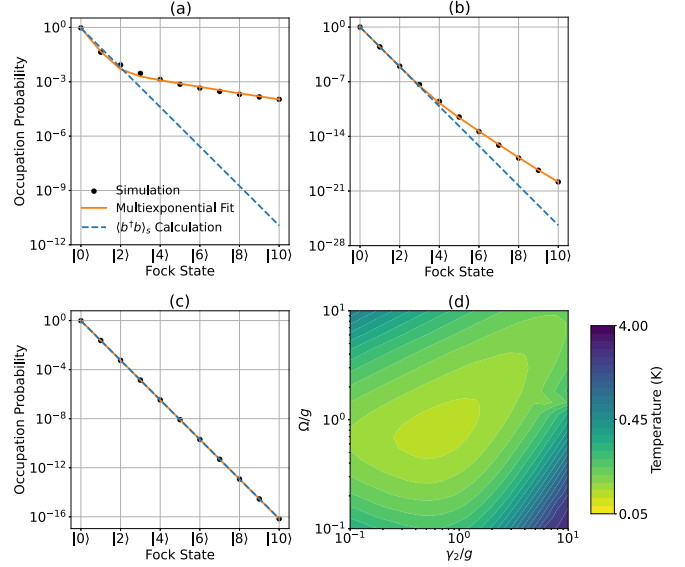


FIG. 8. Regime  $\gamma_1 = \gamma_2$ . The distribution of Fock population is plotted as a function of Fock state number for different pumping strengths and decay rates of the second excited state (a)  $\Omega = 0.2g$ ,  $\gamma_2 = 0.1g$ , (b)  $\Omega = 1.0g$ ,  $\gamma_2 = 1.0g$ , and (c)  $\Omega = 10.0g$ ,  $\gamma_2 = 10.0g$ . (d) Variation of effective temperature at steady state with  $\Omega$  and  $\gamma_2$ . The other parameters are  $G = 5$  GHz,  $g = 0.002G = 10$  MHz,  $\omega_m = 2G$ ,  $\gamma = \omega_m/Q_m = 10^{-7}$  GHz, an initial temperature of 2.63 K corresponding to  $n_{th} = 5$ , and the cutoff for the phonon Fock state  $N = 10$ .

Similar to the preceding section, we also include the effect of pure dephasing observed in this quantum-dot system [57] by adding the relevant terms to the master equation. We notice that the additional decoherence reduces the net achievable cooling and shifts the optimized parameter range (Appendix J 1). As opposed to CdSe quantum dots ( $\gamma_1 \ll \gamma_2$  regime), the dephasing rate for InGaAs quantum dots ( $\gamma_1 = \gamma_2$  regime) reported in the literature is higher than the coupling strength  $g$ . Therefore, the optimized parameter range shifts in order to account for the additional decoherence. We further include a small above-band incoherent pump to the polaritonic states, consistent with experiments probing polaritons [58] by adding the terms  $\gamma_p \mathcal{L}[\sigma_{10}]\rho$  and  $\gamma_p \mathcal{L}[\sigma_{20}]\rho$  to the master Eq. (3), where  $\gamma_p$  is the incoherent pumping rate. Solving the modified master equation in the steady state, we observe that the optimal values of  $\Omega$  and  $\gamma_2$  increase to compensate for the effect of the above-band incoherent pumping (Appendix J 2).

*Effective temperature.* We calculate the effective temperature for this regime following the same procedure as in Sec. III A. We plot the simulated Fock state occupation probabilities in steady state as black markers and the multiexponential fit Eq. (8) as orange curves in Figs. 8(a)–8(c). Similar to the previous regime, the multiexponential fit reveals that there is one dominant exponential term, i.e.,  $c_1 \sim 1$ . Therefore, we assign an effective temperature to the mechanical mode  $T = 1/\beta_1 k_B$  and plot it as a function of the pumping strength  $\Omega$  and decay rate  $\gamma_2$  in Fig. 8(d). Using the already calculated steady-state average phonon numbers [Fig. 7(b)], we also backcalculate the temperature of the mechanical mode, assuming it to be in a thermal state [probability dis-

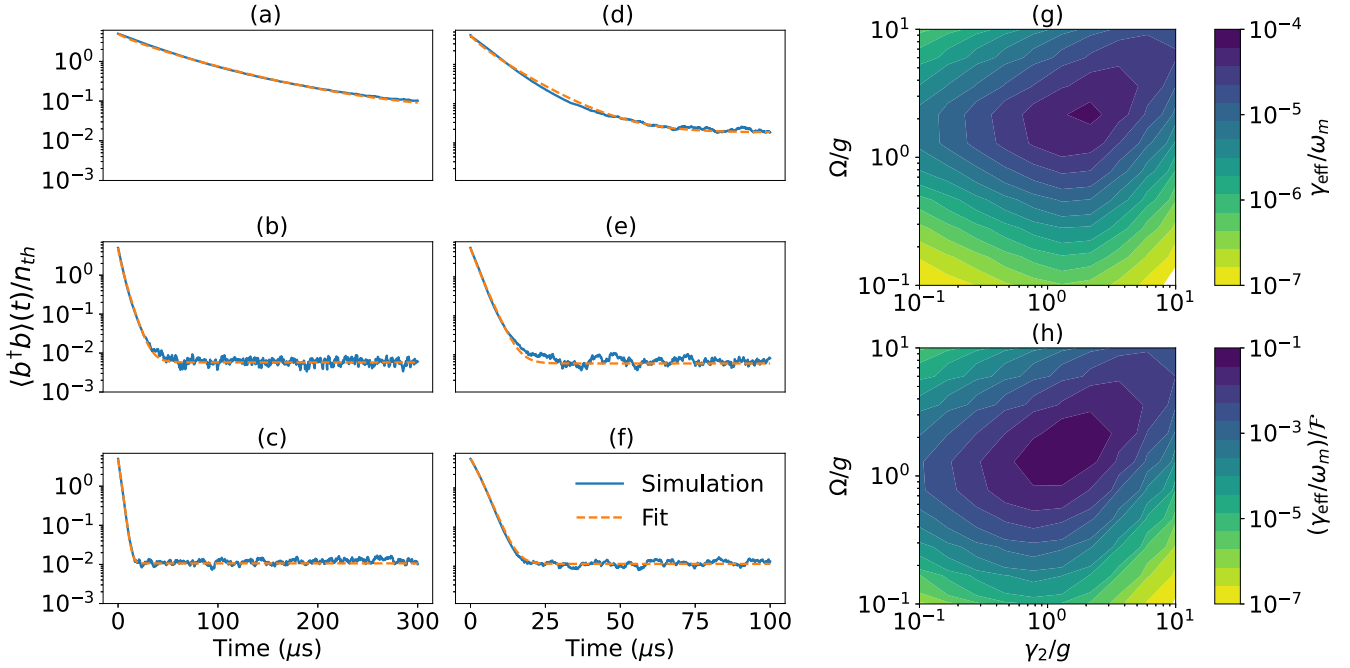


FIG. 9. Regime  $\gamma_1 = \gamma_2$ . Time-dependent decay of the average phonon number of the mechanical mode and the corresponding stretched-exponential fit are shown for (a)  $\Omega = 0.25g$  and  $\gamma_2 = 2g$ , (b)  $\Omega = 1g$  and  $\gamma_2 = 2g$ , (c)  $\Omega = 4g$  and  $\gamma_2 = 2g$ , (d)  $\Omega = 2g$  and  $\gamma_2 = 0.25g$ , (e)  $\Omega = 2g$  and  $\gamma_2 = 1g$ , and (f)  $\Omega = 2g$  and  $\gamma_2 = 4g$ . Also shown are (g)  $\gamma_{eff}/\omega_m$  and (h)  $(\gamma_{eff}/\omega_m)/\mathcal{F}$ , over a range of values of  $\Omega$  and  $\gamma_2$ . The other parameters are  $G = 5$  GHz,  $g = 0.002G = 10$  MHz,  $\omega_m = 2G$ ,  $\gamma = \omega_m/Q_m = 10^{-7}$  GHz, an initial temperature of 2.63 K corresponding to  $n_{th} = 5$ , the cutoff for the phonon Fock state  $N = 65$ , and 500 Monte Carlo trajectories.

tribution shown by blue dashed lines in Figs. 8(a)–8(c)]. The calculated temperature and the effective temperature match well for this regime too. At the optimal pumping strength and optimal decay rate, the effective temperature reduces from 2.63 K to 0.08 K, showing cooling of the mechanical mode by a factor of 32.8.

**Cooling rate.** With the optimization in place, we now proceed to calculate the effective decay rate for the mechanical resonator mode. We choose the same fit function as in Eq. (9) and similar initial conditions: a ground state for the polariton system and a thermal state for the mechanical resonator mode. Figures 9(a)–9(f) show variation of phonon number with time for different values of  $\Omega$  and  $\gamma_2$ , and the associated fits. The extracted value of  $\beta$  for the fits is in  $[0.7, 1)$ , thus revealing the presence of a multiexponential decay. The mean absolute percentage error is less than 5% for all the fits. Figure 9(g) shows the dependence of  $\gamma_{eff}/\omega_m$  over a range of values of  $\Omega$  and  $\gamma_2$ . We also plot the ratio of  $\gamma_{eff}/\omega_m$  to  $\mathcal{F}$  in Fig. 9(h). Similar to the  $\gamma_1 \ll \gamma_2$  regime, a large value of the ratio simultaneously leads to a maximum and efficient cooling of the mechanical mode.

Another system that satisfies the condition  $\gamma_1 = \gamma_2$  is an InAs/GaAs quantum dot doped with a single manganese atom. At low temperatures (approximately 4 K), the excitations of the higher-energy states can be neglected and the system is approximated as a four-level system, comprising two ground states and two excited states, in the absence of a magnetic field [59,60]. In line with the cooling procedure described in Sec. II, we assume that the two excited states couple to a mechanical resonator mode and the first excited state is pumped coherently from the lowest-energy ground

state. This leaves the higher-energy ground state decoupled from the cooling process. We show that the four-level system can be approximated as a three-level system for permitted values of system parameters and therefore follows the optimization method outlined in this section and cools the coupled mechanical mode (Appendix K).

#### IV. CONCLUSION

We have proposed cooling of a mechanical resonator mode using quantum dots. We formulated an optimization problem, using the master-equation approach, over a broad range of system parameters including detunings, decay rates, coupling strengths, and pumping rates. Through particular examples of two quantum-dot systems, i.e., colloidal and epitaxial quantum dots, with mechanical-mode frequencies ranging from megahertz to gigahertz, we showed that ground-state cooling of the mechanical mode is achieved by optimizing the system parameters. We also calculated the cooling rate by estimating the rate of phonon decay and showed that the optimized system parameters simultaneously result in both maximum and efficient cooling. We note that the cooling is robust to small variations in the optimized system parameters because of delocalized maxima observed in Figs. 6(h) and 9(h).

While some previous works have looked at selective optimization of system parameters, our model provides optimization over a broad range of multiple parameters. For example, our model is a generalization to the model presented in [22], where the three-level system was effectively reduced to a two-level system on application of a strong incoherent pump to the first excited state. Replacing the coherent pump



TABLE I. Comparison between our work and the existing literature. Here NV denotes nitrogen vacancy.

Reference	Solid-state system	Parameter(s) optimized
[19]	color center in hBN membrane	coupling strength
[20]	NV center in diamond	detuning
[22]	two-level system (quantum dot, superconducting qubit, NV centers)	decay rates
[23]	superconducting flux qubit	detuning
[26]	quantum dot	detuning
[28]	quantum dots, superconducting qubits, electronic spin qubits	detuning, decay rates
[29]	quantum dots	coupling strength, decay rates
[30]	electromagnetic cavity	coupling strength
[31]	optomechanical cavity	coupling strength
[32]	optomechanical cavity	detuning, coupling strength
[33]	optomechanical cavity	detuning, coupling strength
[34]	optomechanical cavity	detuning, coupling strength
[35]	optomechanical cavity	detuning, coupling strength
present work	quantum dots	detuning, coupling strength, decay rates, pumping strength

with an incoherent pump, our model reproduces the result of [22] for the case of a single atom, giving the optimal decay rate  $\gamma_{2o} = 2g$  (Appendix L). Accounting for experimental limitations, our work provides a generalized framework for optimizing ground-state cooling of a mechanical resonator mode using a quantum dot.

#### ACKNOWLEDGMENTS

We acknowledge financial support from Indo-French Centre for the Promotion of Advanced Research through Project No. 64T3-2. We thank H. Wanare, O. Krebs, S. Ghosh, and S. Shukla for insightful discussions.

#### APPENDIX A: COMPARISON WITH EXISTING LITERATURE

We tabulate the comparison of our work with the existing literature in Table I.

#### APPENDIX B: CONVERSION OF THE HAMILTONIAN TO A ROTATED FRAME

Using a unitary transformation, defined by  $\mathbf{U} = e^{-i\mathbf{H}_o t/\hbar}$ , we transform our system Hamiltonian  $\mathbf{H}_{\text{system}}$  to  $\mathbf{H}_{\text{rotated}} = \mathbf{U}^\dagger \mathbf{H}_{\text{system}} \mathbf{U} - \mathbf{H}_o$  into a new rotating frame of Ref. [61]. We choose  $\mathbf{H}_o = \alpha \sigma_{11} + \beta \sigma_{22} + \zeta b^\dagger b$  and determine  $\alpha = \omega_p$ ,  $\beta = \omega_p + \omega_m$ , and  $\zeta = \omega_m$  such that the rotated Hamiltonian takes the time-independent form Eq. (2).

#### APPENDIX C: HEISENBERG OPERATOR EQUATIONS

The master Eq. (3) can also be written in the Heisenberg picture to calculate the time evolution of an operator  $\mathcal{A}$ ,

$$\begin{aligned} \frac{d\mathcal{A}}{dt} = & -i[\mathcal{A}, \mathbf{H}_{\text{rotated}}] + \gamma_1 \mathcal{L}'[\sigma_{01}]\mathcal{A} + \gamma_2 \mathcal{L}'[\sigma_{02}]\mathcal{A} \\ & + \gamma(n_{\text{th}} + 1)\mathcal{L}'[b]\mathcal{A} + \gamma n_{\text{th}}\mathcal{L}'[b^\dagger]\mathcal{A}, \end{aligned} \quad (\text{C1})$$

where  $\mathcal{L}'[\mathcal{O}]\mathcal{A} = \mathcal{O}\mathcal{A}\mathcal{O}^\dagger - (\mathcal{O}^\dagger\mathcal{O}\mathcal{A} + \mathcal{A}\mathcal{O}^\dagger\mathcal{O})/2$ . Using this equation, we calculate the rate equations for  $b^\dagger b$  and  $\sigma_{22}$

operators. Taking the expectation on both sides of the rate equations, we obtain the rate Eqs. (4).

#### APPENDIX D: FOCK STATE CUTOFF

We observe that choosing a large cutoff is particularly important for reliable evolution of the system dynamics. Since the QUTIP solver `mesolve` is not reliable at large cutoffs (results in negative eigenvalues for the density matrix for several parameter values), we use the Monte Carlo solver `mcsolve`. The Monte Carlo solver evolves an ensemble of wave functions rather than the density matrix [62,63] and therefore it does not suffer from the problem of negative eigenvalues even for large cutoff for the Fock state basis. To evolve the initial thermal state of the system using the Monte Carlo method, we adopt the following approach: Choose a Fock state  $|i\rangle$  and evolve it to get the corresponding density matrix. We then take an average over the density matrix of all Fock states weighted by the thermal state eigenvalues. This approach is possible because the time-evolution superoperator [64] acts linearly on the density matrix as

$$\begin{aligned} \rho(0) &= \sum_i \frac{e^{-n\beta\omega_m}}{Z(\beta)} |i\rangle\langle i| \otimes |0\rangle_q\langle 0|_q, \\ e^{\mathcal{L}t} \rho(0) &= \sum_i \frac{e^{-n\beta\omega_m}}{Z(\beta)} e^{\mathcal{L}t} (|i\rangle\langle i| \otimes |0\rangle_q\langle 0|_q), \\ \rho(t) &= \sum_i \frac{e^{-n\beta\omega_m}}{Z(\beta)} \rho_i(t), \end{aligned}$$

where  $\mathcal{L}$  is the Liouvillian superoperator for time evolution i.e.,  $\dot{\rho} = \mathcal{L}\rho = i[\rho, H] + \sum_i \gamma_i \mathcal{L}[L_i]\rho$ ,  $|0\rangle_q$  denotes the ground state of the quantum dot or polariton,  $\rho_i(t)$  is the density matrix corresponding to the stochastic evolution of  $|i\rangle \otimes |0\rangle_q$ ,  $\beta$  is the inverse temperature,  $\omega_m$  is the mechanical resonator frequency, and  $Z(\beta) = 1/(1 - e^{-\beta\omega_m})$ . We choose an appropriate number of trajectories and cutoff for the phonon Fock state, i.e.,  $N = 20$  and 5000 trajectories for regime  $\gamma_1 \ll \gamma_2$  and  $N = 65$  and 500 trajectories for regime  $\gamma_1 = \gamma_2$ , to

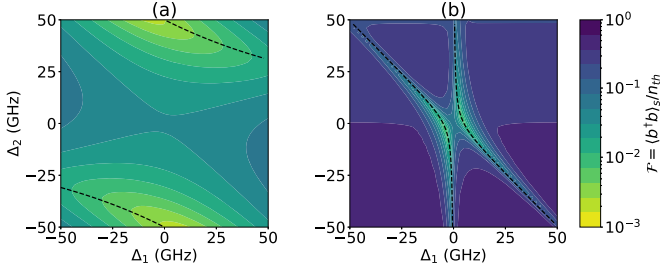


FIG. 10. Variation of  $\mathcal{F} = \langle b^\dagger b \rangle / n_{\text{th}}$  with detunings  $\Delta_1$  and  $\Delta_2$  for two different regimes: (a)  $\Omega = 10g$ , where the black dashed curves represent the analytically derived optimal detuning expression as in Eq. (E1), and (b)  $\Omega = 10^{-1}g$ , where the black dashed curves represent the analytically derived optimal detuning expressions as in Eq. (E2). The other parameters are  $g = 5$  GHz,  $\omega_2 - \omega_1 = 120.9$  GHz,  $\gamma_2 = g/2$ ,  $\gamma_1 = 10^{-1}g$ ,  $\gamma = 10^{-4}g$ , an initial temperature of 50 K, and the cutoff for the mechanical resonator Fock state basis  $N = 10$ .

ensure convergence and consistency of results across different solvers.

We also observe that the steady-state calculations (parameter optimization and effective temperature analysis) converge to true values for a much smaller cutoff as compared to the time-dynamic calculations. The reason for this behavior lies in the fact that the steady-state phonon number  $\langle b^\dagger b \rangle_{\text{ss}}$  is small enough such that only a few Fock state basis are sufficient for its convergence to its true value. Therefore, we choose a lower cutoff ( $N = 10$ ) where the master-equation solver is reliable for all parameter ranges. Moreover, we ensure the convergence of the steady-state phonon number  $\langle b^\dagger b \rangle_{\text{ss}}$  to its true value for the chosen cutoff. We would like to point out that performing steady-state analysis using the Monte Carlo solver is computationally very expensive and results in the same phonon-number values as with the master-equation solver with an  $N = 10$  cutoff, where the master-equation solver is reliable. Therefore, we instead choose the master-equation solver for the steady-state calculations.

#### APPENDIX E: VARIATION OF $\mathcal{F}$ IN THE REGIME $\Omega \not\approx g$

Here we discuss the variation of  $\mathcal{F}$  with detunings and decay rates for two other cases:  $\Omega \gg g$  and  $g \gg \Omega$ . We assume

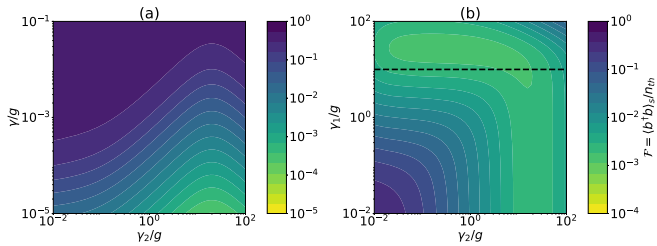


FIG. 11. Variation of  $\mathcal{F}$  with (a) phonon decay rate  $\gamma$  and decay rate of the second excited state  $\gamma_2$  for  $\gamma_1 = 10^{-1}g$  and (b) decay rate of the first excited state  $\gamma_1$  and the second excited state  $\gamma_2$  for  $\gamma = 10^{-4}g$ . The horizontal black dashed line denotes  $\gamma_1 = \Omega$ . The other parameters are  $g = 5$  GHz,  $\Delta_1 = \Delta_2 = 0$ ,  $\omega_2 - \omega_1 = 120.9$  GHz,  $\Omega = 10g$ , an initial temperature of 50 K, and the cutoff for the mechanical resonator Fock state basis  $N = 10$ .

the relative order of magnitude of the detunings  $\Delta_1$  and  $\Delta_2$  to be similar to the coherent interaction strengths  $g$  and  $\Omega$ .

#### 1. Detunings

In the regime  $\Omega \gg g$  or  $g \gg \Omega$ , we neglect the non-dominant coherent process in the rotated Hamiltonian and subsequently calculate the eigenenergies and the modified detunings. To obtain the optimal detuning conditions, these modified detunings should be set to zero for the resonant interaction.

When  $\Omega \gg g$ , the eigenenergies of the rotated Hamiltonian, neglecting the Jaynes-Cummings phonon coupling term, are  $\omega_{\pm} = \Delta_1/2 \pm \sqrt{\Delta_1^2/4 + \Omega^2}$  and  $\omega_2 = \Delta_1 + \Delta_2$ . The second excited state  $|2\rangle$  now couples to both dressed states. The modified detunings are  $\Delta_{\pm} = \omega_2 - \omega_{\pm} = \Delta_2 + \Delta_1/2 \mp \sqrt{\Delta_1^2/4 + \Omega^2}$ . Setting them to zero gives the optimal detuning condition

$$\Delta_2 = -\Delta_1/2 \pm \sqrt{\Delta_1^2/4 + \Omega^2}. \quad (\text{E1})$$

For the case  $g \gg \Omega$ , neglecting the pumping term and calculating the eigenenergies gives  $\omega_o = 0$  and  $\omega_{\pm} = \Delta_1 + \Delta_2/2 \pm \sqrt{\Delta_2^2/4 + g^2}$ . The modified detunings  $\Delta_{\pm} = \omega_{\pm} - \omega_o = \Delta_1 + \Delta_2/2 \pm \sqrt{\Delta_2^2/4 + g^2}$ , when set to zero, give the optimal detuning condition

$$\Delta_1 = -\Delta_2/2 \pm \sqrt{\Delta_2^2/4 + g^2}. \quad (\text{E2})$$

Using the quantum toolbox, we simulate the variation in the figure of merit  $\mathcal{F}$  with  $\Delta_1$  and  $\Delta_2$  in Fig. 10, with the parameters  $\omega_2 - \omega_1 = 120.9$  GHz,  $g = 5$  GHz,  $\gamma_2 = g/2$ ,  $\gamma_1 = 10^{-1}g$ ,  $\gamma = 10^{-4}g$ , and an initial temperature of 50 K. We also plot the analytically derived expressions of optimal detuning as black dashed curves. For the  $\Omega \gg g$  case we set  $\Omega = 10g$  and for the  $g \gg \Omega$  case  $\Omega = 10^{-1}g$ . Both these cases show that minimization of  $\mathcal{F}$  is achievable in the nonresonant system by tuning the pump frequency, which in turn changes  $\Delta_1$ . We observe that the minimum achievable value of  $\mathcal{F}$  in the regime  $\Omega \not\approx g$  obtained by varying the detunings is greater than that in the regime  $\Omega \approx g$ .

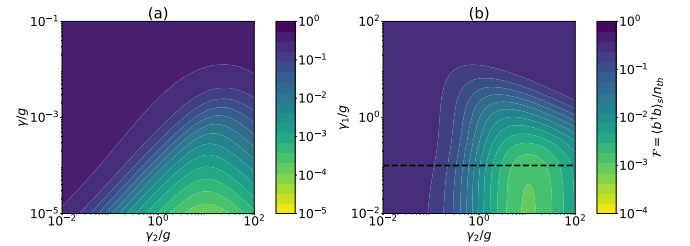


FIG. 12. Variation of  $\mathcal{F}$  with (a) phonon decay rate  $\gamma$  and decay rate of the second excited state  $\gamma_2$  for  $\gamma_1 = 10^{-1}g$  and (b) decay rate of the first excited state  $\gamma_1$  and the second excited state  $\gamma_2$  for  $\gamma = 10^{-4}g$ . The horizontal black dashed line denotes  $\gamma_1 = \Omega$ . The other parameters are  $g = 5$  GHz,  $\Delta_1 = \Delta_2 = 0$ ,  $\omega_2 - \omega_1 = 120.9$  GHz,  $\Omega = 0.1g$ , an initial temperature of 50 K, and the cutoff for the mechanical resonator Fock state basis  $N = 10$ .

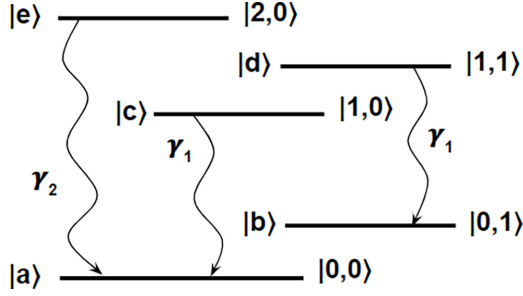


FIG. 13. Combined states for the quantum-dot system and mechanical resonator mode of the form  $|i, j\rangle$ , where indices  $i$  and  $j$  correspond to the quantum-dot system and the mechanical resonator mode, respectively.

## 2. Decay rates

Using the quantum toolbox, we plot the variation of  $\mathcal{F}$  with decay rates for the regime  $\Omega \gg g$  in Fig. 11 and  $g \gg \Omega$  in Fig. 12. Here  $\Delta_1 = \Delta_2 = 0$ . Since the optimal detuning condition is modified in these regimes from  $\Delta_1 = \Delta_2 = 0$  (as discussed in the preceding section), the minimum achievable  $\mathcal{F}$  is greater than in the regime  $\Omega \approx g$ .

In both regimes  $\Omega \gg g$  and  $g \gg \Omega$ , the decay rates  $\gamma$  and  $\gamma_2$  follow the same trend as in Fig. 3. However, in Fig. 11(b) we observe that an optimal  $\gamma_1$  exists in the regime  $\Omega \gg g$ . This can be understood as follows.

(a) A larger value of  $\Omega$  allows for a large  $\gamma_1$  before decoherence sets in.

(b) As discussed in the preceding section, the optimal detuning condition in the regime  $\Omega \gg g$ , which results in resonant interactions, is modified from the current detuning values ( $\Delta_1 = \Delta_2 = 0$ ). To accommodate for the now non-resonant interaction between the eigenstates, the eigenstates require a large linewidth. The linewidth for the eigenstates is proportional to the decay rates  $\gamma_1$  and  $\gamma_2$ . Therefore, under the condition  $\Omega \gtrsim \gamma_1$ ,  $\gamma_1$  can be varied to minimize  $\mathcal{F}$ , leading to an optimal  $\gamma_1$ .

A similar trend is not observed in Fig. 12(b) since  $g \gg \Omega$ , which does not allow room for the tuning of  $\gamma_1$  to minimize  $\mathcal{F}$  without decoherence setting in.

## APPENDIX F: EQUATIONS OF MOTION FOR DENSITY-MATRIX ELEMENTS

We denote the combined states of the quantum-dot system and the mechanical resonator mode by  $|i, j\rangle$ , where indices  $i \in [0, 1, 2]$  and  $j \in [0, 1]$  correspond to the quantum-dot system and the mechanical resonator, respectively (Fig. 13). For brevity, we label the combined state basis as  $|a\rangle, |b\rangle, \dots, |e\rangle$ , as depicted in Fig. 13 by the labels on the left.

Next we derive the equations of motion of various density-matrix elements needed to characterize the dynamics of the combined system completely:

$$\begin{aligned}
 \frac{d\rho_{bb}}{dt} &= i\Omega(\rho_{bd} - \rho_{db}) + \gamma n_{\text{th}}\rho_{aa} - \gamma(n_{\text{th}} + 1)\rho_{bb} + \gamma_1\rho_{dd}, \\
 \frac{d\rho_{cc}}{dt} &= i\Omega(\rho_{ca} - \rho_{ac}) + \gamma(n_{\text{th}} + 1)\rho_{dd} - \gamma n_{\text{th}}\rho_{cc} - \gamma_1\rho_{cc}, \\
 \frac{d\rho_{dd}}{dt} &= ig(\rho_{de} - \rho_{ed}) + i\Omega(\rho_{db} - \rho_{bd}) + \gamma n_{\text{th}}\rho_{cc} \\
 &\quad - \gamma(n_{\text{th}} + 1)\rho_{dd} - \gamma_1\rho_{dd}, \\
 \frac{d\rho_{ee}}{dt} &= ig(\rho_{ed} - \rho_{de}) - \gamma_2\rho_{ee}, \\
 \frac{d\rho_{db}}{dt} &= -ig\rho_{eb} + i\Omega(\rho_{dd} - \rho_{bb}) + \gamma n_{\text{th}}\rho_{ca} - \gamma(n_{\text{th}} + 1)\rho_{db} \\
 &\quad - \frac{\gamma_1}{2}\rho_{db}, \\
 \frac{d\rho_{eb}}{dt} &= -ig\rho_{db} + i\Omega\rho_{ed} - \frac{\gamma_2 + \gamma(n_{\text{th}} + 1)}{2}\rho_{eb}, \\
 \frac{d\rho_{ca}}{dt} &= i\Omega(\rho_{cc} - \rho_{aa}) + \gamma(n_{\text{th}} + 1)\rho_{db} - \frac{\gamma_1}{2}\rho_{ca} - \gamma n_{\text{th}}\rho_{ca}, \\
 \frac{d\rho_{ed}}{dt} &= ig(\rho_{ee} - \rho_{dd}) + i\Omega\rho_{eb} - \frac{\gamma_1 + \gamma_2 + \gamma(n_{\text{th}} + 1)}{2}\rho_{ed}.
 \end{aligned} \tag{F1}$$

We calculate the expression for the steady-state phonon number  $\langle b^\dagger b \rangle_{\text{ss}} = \rho_{bb} + \rho_{dd}$  under the following two conditions: For  $\gamma_1 \ll \gamma_2$ ,

$$\langle b^\dagger b \rangle_{\text{ss}} = \frac{\gamma n_{\text{th}}(2\gamma_2(\gamma_2^2\Omega^2 + g^4 + 4\Omega^4) + \gamma\{\gamma_2^2[(g^2 + 4\Omega^2)n_{\text{th}} + 2(g^2 + 2\Omega^2)] + 4g^2(g^2 + 2\Omega^2)(n_{\text{th}} + 1)\})}{2\gamma_2\{2\gamma_2g^2\Omega^2 + \gamma[(3g^4 + 4g^2\Omega^2 + 8\Omega^4)n_{\text{th}} + 2(g^4 + g^2\Omega^2 + 2\Omega^4) + \gamma_2^2\Omega^2(2n_{\text{th}} + 1)]\}}, \tag{F2}$$

and for  $\gamma_1 = \gamma_2$ ,

$$\begin{aligned}
 \langle b^\dagger b \rangle &= \frac{x}{y}, \\
 x &= \gamma_m(2\gamma_2[\gamma_2^6 + 3g^4\Omega^2 + \gamma_2^4(2g^2 + 9\Omega^2) + \gamma_2^2(g^4 + 2g^2\Omega^2 + 24\Omega^4) + 16\Omega^6] + \gamma_m\{2\gamma_2^4[(11g^2 + 42\Omega^2)n_{\text{th}} \\
 &\quad + 5g^2 + 27\Omega^2] + 4g^2\Omega^2(g^2 + 4\Omega^2)(n_{\text{th}} + 1) + \gamma_2^2[g^4 + 30g^2\Omega^2 + (7g^4 + 16g^2\Omega^2 + 96\Omega^4)n_{\text{th}} + 72\Omega^4] \\
 &\quad + 3\gamma_2^6(5n_{\text{th}} + 3)\}), \\
 y &= 2\gamma_2[2\gamma_2g^2\Omega^2(\gamma_2^2 + 4\Omega^2) + \gamma_m((\gamma_2^2 + 4\Omega^2)[\gamma_2^4 + g^4 + \gamma_2^2(2g^2 + 5\Omega^2) + g^2\Omega^2 + 4\Omega^4] + n_{\text{th}}\{7g^4\Omega^2 \\
 &\quad + 12g^2\Omega^4 + \gamma_2^2[2g^4 + 2\gamma_2^2(\gamma_2^2 + 2g^2 + 9\Omega^2) + 19g^2\Omega^2 + 48\Omega^4] + 32\Omega^6\})].
 \end{aligned} \tag{F3}$$

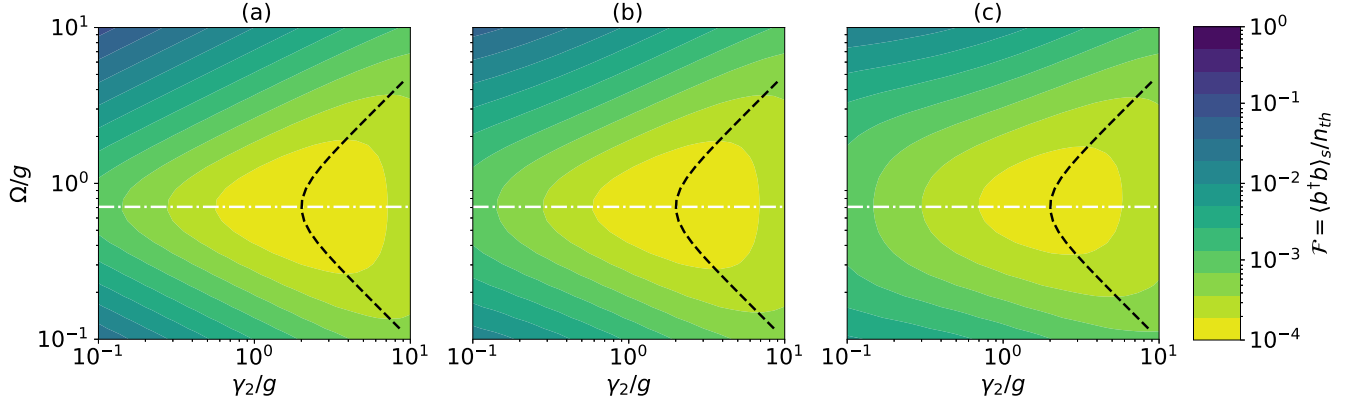


FIG. 14. Regime  $\gamma_1 \ll \gamma_2$ . Variation of  $\mathcal{F}$  with  $\Omega$  and  $\gamma_2$  is shown for different pure dephasing rates  $\gamma_d$ : (a)  $\gamma_d = 0$ , (b)  $\gamma_d = 0.1g$ , and (c)  $\gamma_d = 0.5g$ . The white dot-dashed line and the black dashed curve represent the optimal parameters  $\Omega_o$  and  $\gamma_{2o}$ , respectively, as derived in Eq. (6). The other system parameters are  $\omega_m = 241.8$  GHz,  $g = 20$  GHz,  $\gamma_1 = 10^{-6}$  GHz,  $\gamma = 10^{-3}$  GHz, an initial temperature of 17 K, and the cutoff for the mechanical resonator Fock state basis  $N = 10$ .

### APPENDIX G: EFFECT OF PURE DEPHASING IN THE REGIME $\gamma_1 \ll \gamma_2$

Here we try to discern the effect of pure dephasing on  $\mathcal{F}$  in the regime  $\gamma_1 \ll \gamma_2$  using the quantum toolbox. To do so, we modify the master Eq. (3) to include pure dephasing:

$$\begin{aligned} \frac{d\rho}{dt} = & i[\rho, \mathbf{H}_{\text{rotated}}] + \gamma_1 \mathcal{L}[\sigma_{01}]\rho + \gamma_2 \mathcal{L}[\sigma_{02}]\rho \\ & + \gamma(n_{\text{th}} + 1)\mathcal{L}[b]\rho + \gamma n_{\text{th}}\mathcal{L}[b^\dagger]\rho \\ & + \underbrace{\gamma_d \mathcal{L}[\sigma_{11}]\rho + \gamma_d \mathcal{L}[\sigma_{22}]\rho}_{\text{pure dephasing}}. \end{aligned} \quad (\text{G1})$$

The last two terms account for the pure dephasing process in the excited states  $|1\rangle$  and  $|2\rangle$ , respectively. The Hamiltonian for the system remains the same [Eq. (2)]. In Fig. 14 we plot the variation of  $\mathcal{F}$  with  $\Omega$  and  $\gamma_2$ , for different values of pure dephasing rate  $\gamma_d$  using Eqs. (2) and (G1). The white dot-dashed line and the black dashed curve represent the optimal parameters  $\Omega_o$  and  $\gamma_{2o}$ , respectively, as derived in Eq. (6). For cadmium selenide colloidal quantum dots, the pure dephasing rate  $\gamma_d \approx 10$  GHz =  $g/2$  [39]. We observe that even with the inclusion of the pure dephasing rate, the minimum achievable value for  $\mathcal{F}$  and the optimal values for the parameters  $\Omega$  and  $\gamma_2$  do not change significantly.

### APPENDIX H: EFFECTIVE TEMPERATURE CALCULATION

Since the Fock state occupation probability as a function of Fock state number for the mechanical mode does not necessarily follow an exponential (thermal) distribution, we perform a multiexponential fit as described in Eq. (8). We use the following reasoning: The Fock state occupation distribution plots [Figs. 5 and 8(a)–8(c)] show that when the Fock state occupation distribution is not a straight line, it follows a straight line for the initial few Fock states and also for the final few Fock states albeit with different slopes. This suggests that the Fock state occupation distribution is a sum of at least two exponential terms in which the term with a larger slope

(i.e., inverse temperature) dominates initially and the term with a smaller slope dominates for the higher Fock states. We use the mean absolute percentage error on the logarithmic scale as our measure of the error between the multiexponential function Eq. (8) and the Fock state occupation probability  $P(n)$  values obtained from the QUTIP master-equation solver. The occupation probabilities are extremely small, and hence choosing a logarithmic error helps to avoid floating point errors.

We set the number of terms in the multiexponential function to three [ $k = 3$  in Eq. (8)] since we observe it to be sufficient for errors less than 5%. Before performing a multiexponential fit, however, we check if a single exponential works, i.e., an error of less than 5%. This is because for such cases where the plot is actually a straight line [e.g., Figs. 5(c) and 16(c)], the optimizer obtains  $\beta_1 \approx \beta_2 \approx \beta_3$  since a single  $\beta$  is sufficient to describe the distribution. Doing so also helps us get an idea of  $\Omega$  and  $\gamma_2$  where a multiexponential fit is required and where a single exponential suffices. We set the initial guess for the weights to be  $c_1 = c_2 = c_3 = \frac{1}{3}$ . The initial guess for the  $\beta$  is quite natural: For  $\beta_1$  it is the initial slope of the Fock state occupation distribution i.e., slope corresponding to the first two Fock states; for  $\beta_3$ , it is the final slope of the Fock state occupation distribution, i.e., slope corresponding to the last two Fock states; for  $\beta_2$ , the initial guess we use is the arithmetic mean of the  $\beta_1$  and  $\beta_3$ . Using an optimization routine, we obtain the optimal values for the inverse temperatures along with their weights. The weight and temperature (equal to  $1/\beta_i k_B$ ) maps can be seen in Fig. 15 for the  $\gamma_1 \ll \gamma_2$  regime and in Fig. 16 for the  $\gamma_1 = \gamma_2$  case. The white regions represent the areas where a multiexponential fit was not necessary, i.e., a single exponential was a good fit.

From Figs. 15 and 16(a)–16(c) we observe that the values of  $c_2$  and  $c_3$  obtained from the optimization routine are many orders of magnitude smaller than  $c_1$ , which is approximately 1 for all values of  $\Omega$  and  $\gamma_2$ . This suggests that we can ascribe an effective temperature of  $T_1$  to the mechanical mode.



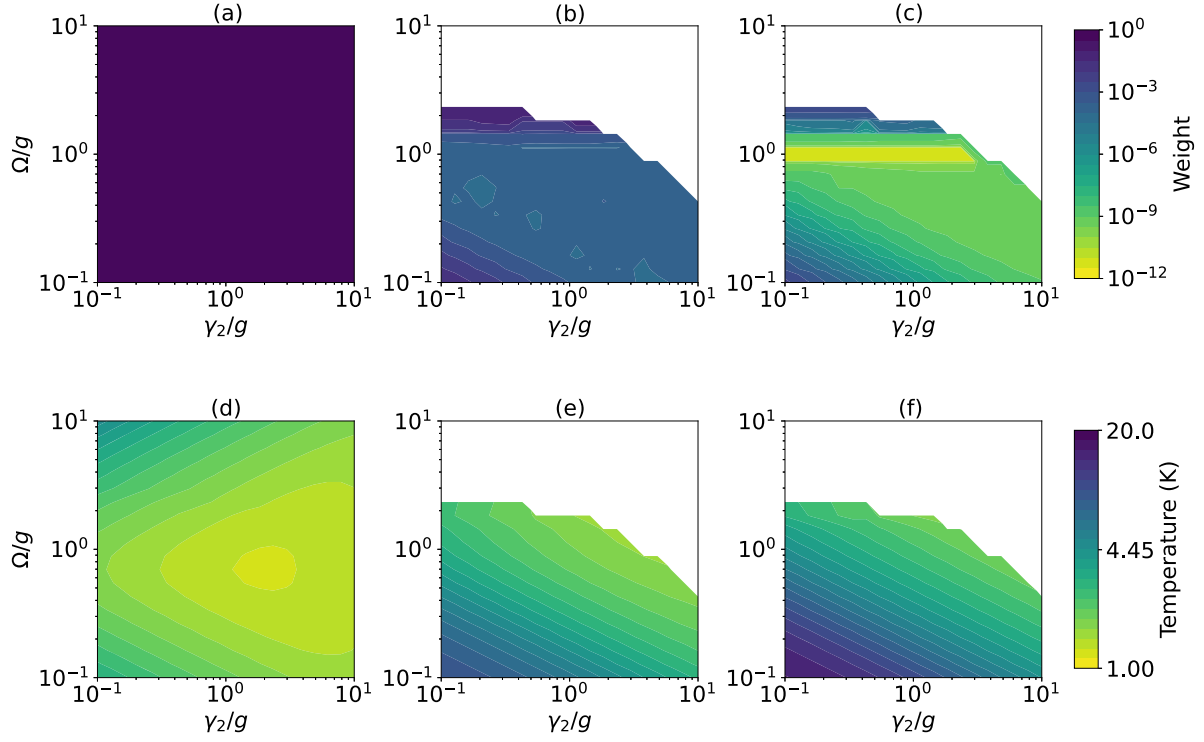


FIG. 15. Regime  $\gamma_1 \ll \gamma_2$ . Shown is the variation, with  $\Omega$  and  $\gamma_2$ , of (a) weight  $c_1$  (note that  $c_1$  takes a value between 0.9 and 1 but the variation is not visible on the logarithmic color scale), (b) weight  $c_2$  ( $c_2 \sim 10^{-5}$ – $10^{-1}$ ), (c) weight  $c_3$  ( $c_3 \sim 10^{-11}$ – $10^{-3}$ ), (d) temperature  $T_1$ , (e) temperature  $T_2$ , and (f) temperature  $T_3$ .

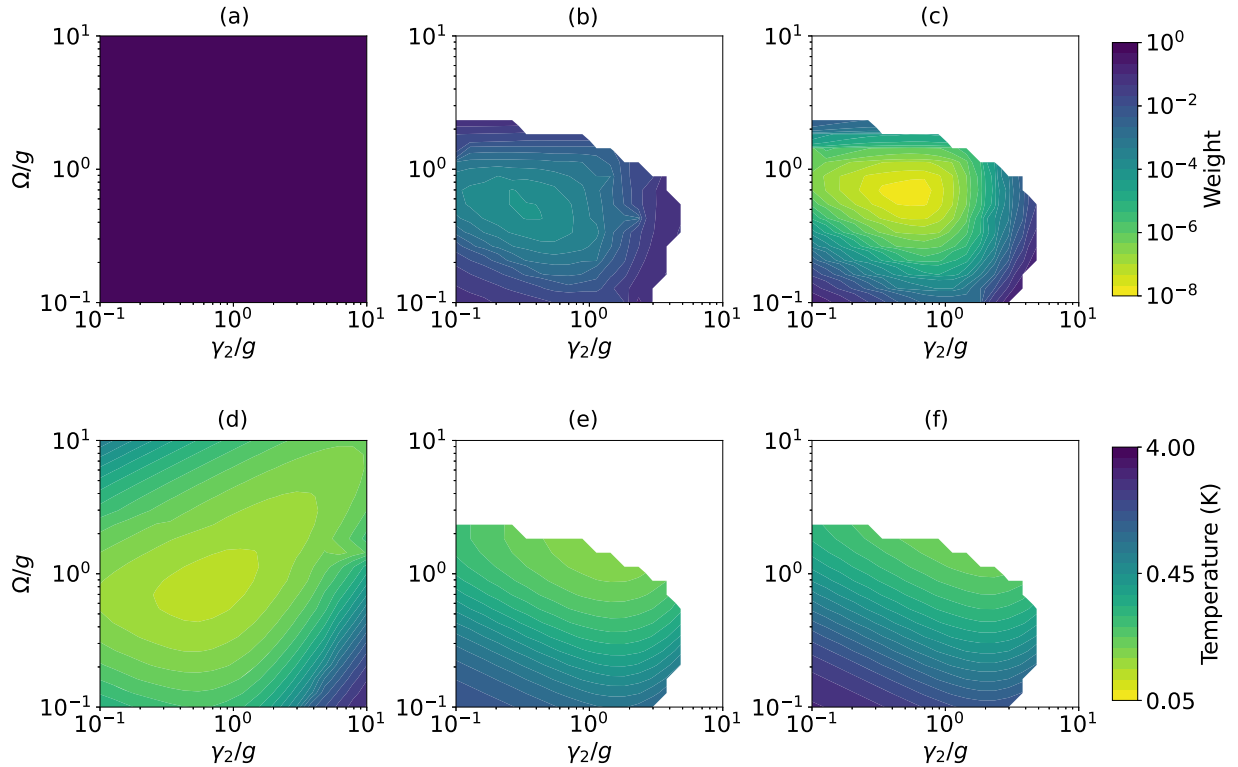


FIG. 16. Regime  $\gamma_1 = \gamma_2$ . Shown is the variation, with  $\Omega$  and  $\gamma_2$ , of (a) weight  $c_1$  (note that  $c_1$  takes a value between 0.85 and 1 but the variation is not visible on the logarithmic color scale), (b) weight  $c_2$  ( $c_2 \sim 10^{-4}$ – $10^{-1}$ ), (c) weight  $c_3$  ( $c_3 \sim 10^{-8}$ – $10^{-1}$ ), (d) temperature  $T_1$ , (e) temperature  $T_2$ , and (f) temperature  $T_3$ .

## APPENDIX I: HAMILTONIAN OF A TLS COUPLED TO AN OPTICAL CAVITY MODE AND A MECHANICAL RESONATOR

The Hamiltonian for a single-mode cavity mode strongly coupled to a two-level system, forming polaritons, which in turn couple to a mode of a mechanical resonator, is given by

$$\begin{aligned} \mathbf{H}_{\text{system}} = & \underbrace{\omega_c a^\dagger a + \omega_\alpha \sigma_{\alpha\alpha} + G(\sigma_{\beta\alpha} a^\dagger + \sigma_{\alpha\beta} a)}_{\mathbf{H}_{\text{JC}}} \\ & + \Omega(\sigma_{\alpha\beta} e^{-i\omega_p t} + \sigma_{\beta\alpha} e^{i\omega_p t}) + \omega_m b^\dagger b + g a^\dagger a (b^\dagger + b), \end{aligned} \quad (\text{I1})$$

where  $|\beta\rangle$  and  $|\alpha\rangle$  are the ground and excited states for the two-level system with frequency separation  $\omega_\alpha$ ,  $a$  ( $b$ ) is the annihilation operator of the cavity (mechanical) mode with frequency  $\omega_a$  ( $\omega_m$ ),  $G$  is TLS-cavity-mode coupling strength,  $\Omega$  is the pumping strength to the TLS at frequency  $\omega_p$ , and  $g$  is optomechanical coupling strength. Following the process as described in Refs. [40,65], we write the system Hamiltonian

in the diagonalized basis of the TLS-cavity Hamiltonian  $\mathbf{H}_{\text{JC}}$ . Restricting the number of photons in the cavity mode to one, the Hamiltonian  $\mathbf{H}_{\text{JC}}$  can be readily diagonalized such that  $\mathbf{H}_{\text{JC}} |\pm\rangle = \omega_\pm |\pm\rangle$ , where

$$|0\rangle = |\beta, 0\rangle, \quad (\text{I2a})$$

$$|- \rangle = -\sin\theta |\alpha, 0\rangle + \cos\theta |\beta, 1\rangle, \quad (\text{I2b})$$

$$|+ \rangle = \cos\theta |\alpha, 0\rangle + \sin\theta |\beta, 1\rangle, \quad (\text{I2c})$$

$$\omega_\pm = \frac{\omega_a + \omega_c}{2} \pm \sqrt{G^2 + \frac{\Delta^2}{4}}. \quad (\text{I2d})$$

Here  $\tan(2\theta) = 2G/\Delta$  and  $\Delta = \omega_\alpha - \omega_a$ . The cavity annihilation operator in the restricted polariton basis can be written as  $a = \sin\theta |\beta, 0\rangle\langle +| + \cos\theta |\beta, 0\rangle\langle -|$  [50] and the number operator as  $a^\dagger a = \sin^2\theta |+\rangle\langle +| + \cos^2\theta |-\rangle\langle -| + \sin\theta \cos\theta (|+\rangle\langle -| + |-\rangle\langle +|)$ . Substituting these relations in Eq. (I1), the system Hamiltonian in the polariton basis becomes

$$\begin{aligned} \mathbf{H}_{\text{system}} = & \omega_- \sigma_{--} + \omega_+ \sigma_{++} + \omega_m b^\dagger b + \Omega[(\cos\theta \sigma_{0+} - \sin\theta \sigma_{0-} + \cos\theta \sin\theta \sigma_{++} + \cos^2\theta \sigma_{-+} - \sin^2\theta \sigma_{+-} \\ & - \cos\theta \sin\theta \sigma_{--}) e^{i\omega_p t} + \text{c.c.}] + g(b + b^\dagger)[\sin^2\theta \sigma_{++} + \cos^2\theta \sigma_{--} + \cos\theta \sin\theta (\sigma_{+-} + \sigma_{-+})]. \end{aligned} \quad (\text{I3})$$

We assume that the applied pump is close to the frequency of the lower polariton ( $\omega_p - \omega_- \approx 0$ ) and that the mechanical resonator frequency is close to the frequency difference between the upper and lower polaritons ( $\omega_+ - \omega_- - \omega_m \approx 0$ ). Because of this, several terms in Eq. (I3) are off-resonant and can be dropped under the rotating-wave approximation. To elucidate this fact, we move to an interaction picture by rotating the Hamiltonian in Eq. (I3) with respect to the Hamiltonian  $H_o = \omega_- \sigma_{--} + \omega_+ \sigma_{++} + \omega_m b^\dagger b$  to obtain

$$\begin{aligned} \mathbf{H}_{\text{rotated}} = & \Omega[(\cos\theta \sigma_{0+} e^{i(\omega_p - \omega_-)t} - \sin\theta \sigma_{0-} e^{i(\omega_p - \omega_-)t} + \cos\theta \sin\theta \sigma_{++} e^{i\omega_p t} + \cos^2\theta \sigma_{-+} e^{i(\omega_- - \omega_+ + \omega_p)t} \\ & - \sin^2\theta \sigma_{+-} e^{i(\omega_+ - \omega_- + \omega_p)t} - \cos\theta \sin\theta \sigma_{--} e^{i\omega_p t}) + \text{c.c.}] + g(b e^{-i\omega_m t} + b^\dagger e^{i\omega_m t})[\sin^2\theta \sigma_{++} + \cos^2\theta \sigma_{--} \\ & + \cos\theta \sin\theta (\sigma_{+-} e^{i(\omega_+ - \omega_-)t} + \sigma_{-+} e^{i(\omega_- - \omega_+)t})]. \end{aligned} \quad (\text{I4})$$

In this equation we keep only the slow rotating terms and drop the fast rotating terms under the rotating-wave approximation. Returning to the nonrotating frame, the combined system Hamiltonian now becomes

$$\begin{aligned} \mathbf{H}_{\text{system}} = & \omega_- \sigma_{--} + \omega_+ \sigma_{++} + \omega_m b^\dagger b - \Omega \sin\theta (\sigma_{0-} e^{i\omega_p t} \\ & + \sigma_{0-} e^{-i\omega_p t}) + g \sin\theta \cos\theta (\sigma_{-+} b + \sigma_{+-} b^\dagger). \end{aligned} \quad (\text{I5})$$

## APPENDIX J: EFFECT OF INCOHERENT PROCESSES IN THE REGIME $\gamma_1 = \gamma_2$

### 1. Pure dephasing

To account for pure dephasing, we use the same formalism as in Appendix G. The dephasing rate for InGaAs quantum dots is reported to be  $\gamma_d = 0.3 \mu\text{eV} = 72.54 \text{ MHz} = 7.25g$  [57]. Using the quantum toolbox, we plot the variation of  $\mathcal{F}$  with  $\Omega$  and  $\gamma_2$ , for different values of pure dephasing rate  $\gamma_d$  in Fig. 17. The effect of pure dephasing is to increase the optimal value of  $\Omega$  and decrease the optimal value of

$\gamma_2$  to account for the additional decoherence. This effect is significant only when the dephasing rate  $\gamma_d$  is of the order of the optomechanical coupling strength  $g$ .

### 2. Above-band pumping

To account for above-band or incoherent pumping, we modify the original master equation to

$$\begin{aligned} \frac{d\rho}{dt} = & i[\rho, \mathbf{H}_{\text{rot}}] + \gamma_1 \mathcal{L}[\sigma_{01}]\rho + \gamma_2 \mathcal{L}[\sigma_{02}]\rho \\ & + \gamma(n_{\text{th}} + 1)\mathcal{L}[b]\rho + \gamma n_{\text{th}}\mathcal{L}[b^\dagger]\rho \\ & + \underbrace{\gamma_p \mathcal{L}[\sigma_{10}]\rho + \gamma_p \mathcal{L}[\sigma_{20}]\rho}_{\text{incoherent pumping}}. \end{aligned} \quad (\text{J1})$$

The last two terms in this equation represent above-band pumping to the excited states  $|1\rangle$  and  $|2\rangle$ , respectively. The Hamiltonian for the system remains the same [Eq. (2)]. We plot the variation of  $\mathcal{F}$  with  $\Omega$  and  $\gamma_2$  using Eqs. (2) and (J1) in Fig. 18 for  $\gamma_p = 0$  [Fig. 18(a)] and  $\gamma_p = 0.01g$  [Fig. 18(b)]. Comparing Figs. 18(a) and 18(b), we observe that the above-band pumping leads to an increase in the minimum value of

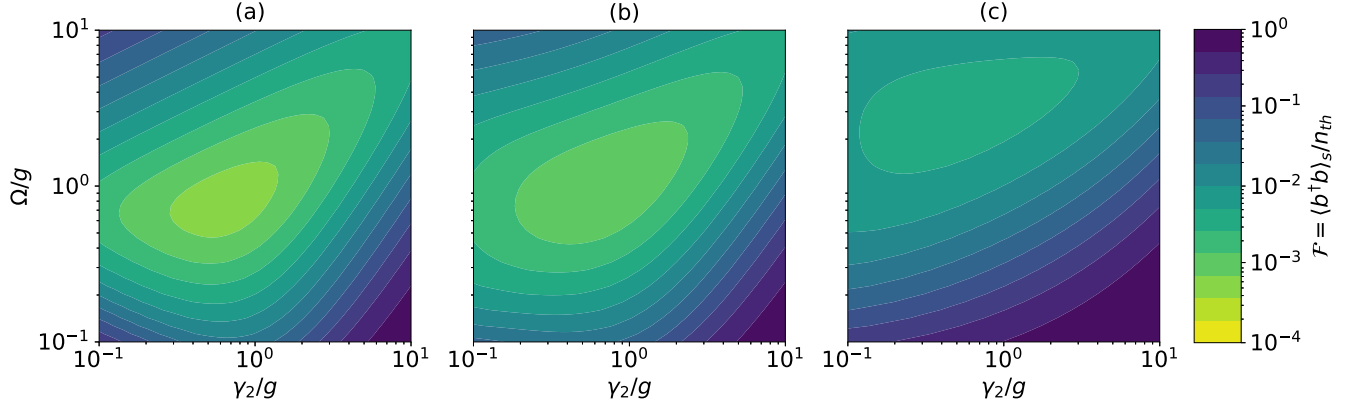


FIG. 17. Regime  $\gamma_1 = \gamma_2$ . Variation of  $\mathcal{F}$  with  $\Omega$  and  $\gamma_2$  is shown for different pure dephasing rates  $\gamma_d$ : (a)  $\gamma_d = 0$ , (b)  $\gamma_d = 0.5g$ , and (c)  $\gamma_d = 7.25g$ . The other system parameters are  $G = 5$  GHz,  $g = 0.002G$ ,  $\omega_m = 2G$ ,  $\gamma = \omega_m/Q_m = 10^{-7}$  GHz, an initial temperature of 2.63 K corresponding to  $n_{\text{th}} = 5$ , and the cutoff for the mechanical resonator Fock state basis  $N = 10$ .

$\mathcal{F}$  and heating ( $\mathcal{F} > 1$ ) for small  $\Omega/g$  and  $\gamma_2/g$ . Furthermore, the optimal values for the parameters  $\Omega$  and  $\gamma_2$  increase. To explain this, we solve the Heisenberg operator equations, including above-band pumping, to write the steady-state phonon occupation

$$\langle b^\dagger b \rangle_{\text{ss}} = n_{\text{th}} - \frac{\gamma_2}{\gamma} \langle \sigma_{22} \rangle_{\text{ss}} + \frac{\gamma_p}{\gamma} \langle \sigma_{00} \rangle_{\text{ss}}. \quad (\text{J2})$$

Compared to Eq. (5), Eq. (J2) has an additional term that is proportional to the above-band pumping rate  $\gamma_p$ . This additional term is responsible for an increase in the steady-state phonon number  $\langle b^\dagger b \rangle_{\text{ss}}$  and therefore  $\mathcal{F} = \langle b^\dagger b \rangle_{\text{ss}} / n_{\text{th}}$ . The minimization problem for  $\mathcal{F}$  is modified, resulting in different optimal parameter values for  $\Omega$  and  $\gamma_2$ . To minimize  $\mathcal{F}$ , the last two terms in Eq. (J2) need to be maximized and minimized simultaneously. Since the above-band pumping rate  $\gamma_p$  is nonzero and fixed, the optimal value for  $\Omega$  needs to be increased to decrease  $\langle \sigma_{00} \rangle_{\text{ss}}$  in order to minimize the last term. Subsequently, a larger  $\gamma_2$  is required to accommodate the increased population transitioning to the state  $|2\rangle$ . This results in increased optimal values for  $\Omega$  and  $\gamma_2$  as compared to when the above-band pumping is absent ( $\gamma_p = 0$ ).

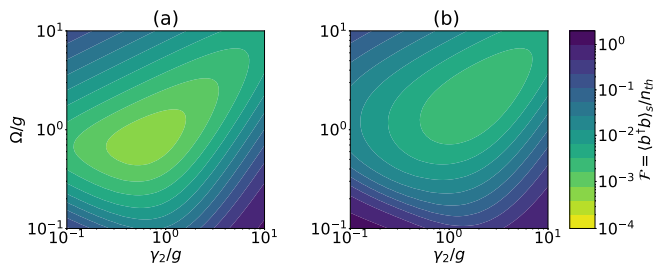


FIG. 18. Regime  $\gamma_1 = \gamma_2$ . Variation of  $\mathcal{F}$  with  $\Omega$  and  $\gamma_2$  is shown for (a)  $\gamma_p = 0$  and (b)  $\gamma_p = 0.01g$ . The other system parameters are  $G = 5$  GHz,  $g = 0.002G$ ,  $\omega_m = 2G$ ,  $\gamma = \omega_m/Q_m = 10^{-7}$  GHz, an initial temperature of 2.63 K corresponding to  $n_{\text{th}} = 5$ , and the cutoff for the mechanical resonator Fock state basis  $N = 10$ .

## APPENDIX K: COOLING OF A MECHANICAL MODE COUPLED TO A MANGANESE-DOPED QUANTUM DOT

Similar to Sec. II, we label the states  $|0\rangle, |1\rangle, |2\rangle, |3\rangle$  as shown in Fig. 19. Moving to a suitable rotated frame of reference, the system Hamiltonian can be simplified to

$$\begin{aligned} \mathbf{H}_{\text{rotated}} = & \Delta_1 \sigma_{11} + (\Delta_1 + \Delta_2) \sigma_{22} + \omega_3 \sigma_{33} + \Omega(\sigma_{01} + \sigma_{10}) \\ & + g(\sigma_{12} b^\dagger + \sigma_{21} b). \end{aligned} \quad (\text{K1})$$

Here  $\Delta_1 = \omega_1 - \omega_p$ ,  $\Delta_2 = \omega_2 - \omega_1 - \omega_m$ ,  $g$  is the coupling strength of the two excited states with the mechanical mode of frequency  $\omega_m$ , and  $\Omega$  is the coherent pumping strength between the states  $|0\rangle$  and  $|1\rangle$  at frequency  $\omega_p$ . The excited states  $|1\rangle$  and  $|2\rangle$  decay to both the ground states  $|0\rangle$  and  $|3\rangle$  with equal decay rate, which we denote by  $\gamma_2$ . Furthermore, the higher-energy ground state  $|3\rangle$  also decays to the lower-energy ground state  $|0\rangle$  with rate  $\gamma_3$ . The master equation for the system, taking into account all the incoherent processes, is

$$\begin{aligned} \frac{d\rho}{dt} = & i[\rho, \mathbf{H}_{\text{rotated}}] + \gamma_2(\mathcal{L}[\sigma_{01}]\rho + \mathcal{L}[\sigma_{02}]\rho + \mathcal{L}[\sigma_{31}]\rho \\ & + \mathcal{L}[\sigma_{32}]\rho) + \gamma_3\mathcal{L}[\sigma_{03}]\rho + \gamma(n_{\text{th}} + 1)\mathcal{L}[b]\rho \\ & + \gamma n_{\text{th}}\mathcal{L}[b^\dagger]\rho + \gamma_d\mathcal{L}[\sigma_{11}]\rho + \gamma_d\mathcal{L}[\sigma_{22}]. \end{aligned} \quad (\text{K2})$$

The last two terms in Eq. (K2) account for the pure dephasing in the excited states. Consistent with Ref. [60], we set

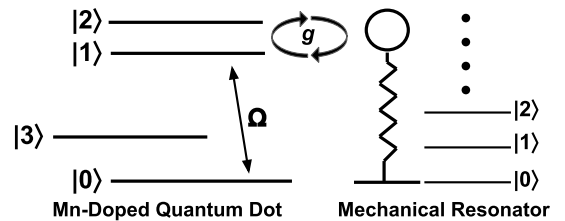


FIG. 19. Schematic representing a manganese-doped quantum dot coupled to a mode of a mechanical resonator.

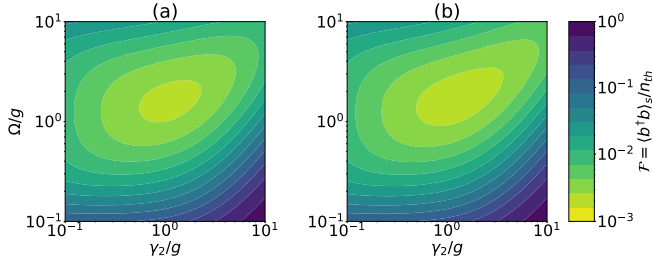


FIG. 20. Variation of  $\mathcal{F}$  with  $\Omega$  and  $\gamma_2$  as per (a) the four-level Mn-doped quantum-dot model and (b) the  $\gamma_1 = \gamma_2$  regime formulation described in Sec. III B. The system parameters are  $\omega_3 = 170$  GHz,  $g = 10$  MHz,  $\omega_m = 35$  GHz,  $\gamma_3 = \gamma_d = 24.18$  MHz,  $Q_m = 10^7$ , an initial temperature of 5 K corresponding to  $n_{\text{th}} = 2.52$ , and the cutoff for the Fock states  $N = 10$ .

$\omega_3 = 170$  GHz,  $\omega_m = 35$  GHz, and  $\gamma_3 = \gamma_d = 24.18$  MHz. The system affords decay and dephasing rates of the order of 10 MHz because of the highly delocalized nature of the Mn dopant complex in the quantum dot. We further set  $\Delta_1 = \Delta_2 = 0$ ,  $g = 10$  MHz, and the mechanical quality factor  $Q_m = \omega_m/\gamma_m = 10^7$ . Similar to our previous formulations, the control parameters in this model are the pumping strength  $\Omega$  and the decay rate of the excited states  $\gamma_2$ . The decay rate of the excited states can be increased (decreased) simultaneously via Purcell enhancement (suppression) by coupling to two different modes of the same optical cavity. Using the quantum toolbox, we solve the master Eq. (K2) and calculate  $\mathcal{F}$ . In Fig. 20(a) we plot the variation of  $\mathcal{F}$  with  $\Omega$  and  $\gamma_2$  for the full four-level system model. In comparison, using the same parameters, we plot  $\mathcal{F}$  in the limit  $\gamma_3 \rightarrow \infty$ , thereby reducing the four-level system to a three-level system, in Fig. 20(b). This is equivalent to the formulation described in Sec. III B (regime  $\gamma_1 = \gamma_2$ ).

We observe that both models are in good agreement except when  $\Omega, \gamma_2 > g$ . This can be understood as follows. The finite steady-state population of the state  $|3\rangle$  that is not involved in the cooling dynamics leads to a disagreement between the two models. For the figure of merit  $\mathcal{F}$  to be equivalent in both the models, the steady-state population of the higher-energy ground state  $\langle\sigma_{33}\rangle_{\text{ss}}$  should be as small as possible. In the limit  $\gamma_3 \rightarrow \infty$ ,  $\langle\sigma_{33}\rangle_{\text{ss}} \rightarrow 0$  and the four-level system exactly mimics a three-level system. As the value of  $\gamma_3$  is finite and fixed, other system parameters need to be taken into account

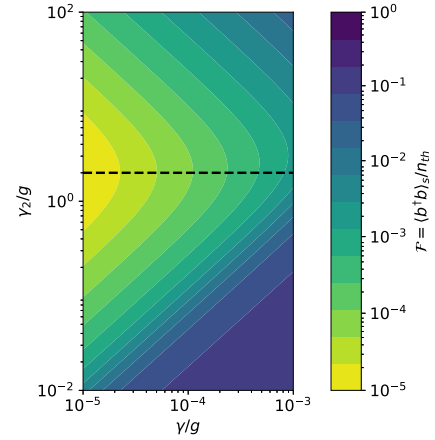


FIG. 21. Variation of  $\mathcal{F}$  with the decay rate of the second excited state  $\gamma_2$  and phonon decay rate  $\gamma$  under strong incoherent pumping. The black dashed line represents the optimal decay rate as obtained from our model. The parameters are  $\omega_m = 200$  MHz,  $n_{\text{th}} \approx 200$ ,  $g = 1$  MHz,  $\gamma_p = 10g$ ,  $\gamma_1 = 10^{-5}g$ , and the cutoff for the mechanical resonator Fock state basis  $N = 300$ .

to determine the validity of the approximation. In the regime  $\Omega > g$  and  $\gamma_2 > g$ , the first condition ensures that the state  $|0\rangle$  is sparsely populated, thus pumping the population to the first excited state  $|1\rangle$ . The second condition leads to an increased population of the state  $|3\rangle$  because of a strong decay from the excited states. When both of these parameter regimes act together, it leads to a disagreement between the two models, as can be seen in the top right corners of Figs. 20(a) and 20(b). In all other ranges of values for  $\Omega$  and  $\gamma_2$ , the two models are in good agreement, thus justifying the approximation of reducing the four-level system to a three-level system.

#### APPENDIX L: OPTIMIZING COOLING IN THE PRESENCE OF STRONG INCOHERENT PUMPING

Following Ref. [22], we set  $\omega_m = 200$  MHz,  $n_{\text{th}} \approx 200$ , and  $g = 1$  MHz and assume  $\gamma_1 = 10^{-5}g$  and  $\gamma_p = 10g$ . Using the quantum toolbox, we plot the variation of  $\mathcal{F}$  as a function of the phonon decay rate  $\gamma$  and the decay rate of the second excited state  $\gamma_2$  in Fig. 21. The black dashed line represents the line  $\gamma_2 = 2g$ , the optimal decay rate obtained from analytical calculations. The results are in good agreement with the results obtained in [22] for the case of a single atom.

- [1] K. C. Schwab and M. L. Roukes, Putting mechanics into quantum mechanics, *Phys. Today* **58**(7), 36 (2005).
- [2] M. Aspelmeyer and K. Schwab, Focus on mechanical systems at the quantum limit, *New J. Phys.* **10**, 095001 (2008).
- [3] J. D. Teufel, T. Donner, M. A. Castellanos-Beltran, J. W. Harlow, and K. W. Lehnert, Nanomechanical motion measured with an imprecision below that at the standard quantum limit, *Nat. Nanotechnol.* **4**, 820 (2009).
- [4] A. G. Krause, M. Winger, T. D. Blasius, Q. Lin, and O. Painter, A high-resolution microchip optomechanical accelerometer, *Nat. Photonics* **6**, 768 (2012).

- [5] Y.-W. Hu, Y.-F. Xiao, Y.-C. Liu, and Q. Gong, Optomechanical sensing with on-chip microcavities, *Front. Phys.* **8**, 475 (2013).
- [6] T. P. Purdy, R. W. Peterson, and C. A. Regal, Observation of radiation pressure shot noise on a macroscopic object, *Science* **339**, 801 (2013).
- [7] L. F. Buchmann, H. Jing, C. Raman, and P. Meystre, Optical control of a quantum rotor, *Phys. Rev. A* **87**, 031601(R) (2013).
- [8] Y.-D. Wang and A. A. Clerk, Using interference for high fidelity quantum state transfer in optomechanics, *Phys. Rev. Lett.* **108**, 153603 (2012).



- [9] V. Fiore, Y. Yang, M. C. Kuzyk, R. Barbour, L. Tian, and H. Wang, Storing optical information as a mechanical excitation in a silica optomechanical resonator, *Phys. Rev. Lett.* **107**, 133601 (2011).
- [10] M. Schmidt, M. Ludwig, and F. Marquardt, Optomechanical circuits for nanomechanical continuous variable quantum state processing, *New J. Phys.* **14**, 125005 (2012).
- [11] K. Stannigel, P. Komar, S. J. M. Habraken, S. D. Bennett, M. D. Lukin, P. Zoller, and P. Rabl, Optomechanical quantum information processing with photons and phonons, *Phys. Rev. Lett.* **109**, 013603 (2012).
- [12] O. Romero-Isart, A. C. Pflanzner, F. Blaser, R. Kaltenbaek, N. Kiesel, M. Aspelmeyer, and J. I. Cirac, Large quantum superpositions and interference of massive nanometer-sized objects, *Phys. Rev. Lett.* **107**, 020405 (2011).
- [13] P. Sekatski, M. Aspelmeyer, and N. Sangouard, Macroscopic optomechanics from displaced single-photon entanglement, *Phys. Rev. Lett.* **112**, 080502 (2014).
- [14] B. Pepper, R. Ghobadi, E. Jeffrey, C. Simon, and D. Bouwmeester, Optomechanical superpositions via nested interferometry, *Phys. Rev. Lett.* **109**, 023601 (2012).
- [15] M. P. Blencowe, Effective field theory approach to gravitationally induced decoherence, *Phys. Rev. Lett.* **111**, 021302 (2013).
- [16] Y.-l. Liu, C. Wang, J. Zhang, and Y.-x. Liu, Cavity optomechanics: Manipulating photons and phonons towards the single-photon strong coupling, *Chin. Phys. B* **27**, 024204 (2018).
- [17] C. Reinhardt, T. Müller, A. Bourassa, and J. C. Sankey, Ultralow-noise SiN trampoline resonators for sensing and optomechanics, *Phys. Rev. X* **6**, 021001 (2016).
- [18] R. A. Norte, J. P. Moura, and S. Gröblacher, Mechanical resonators for quantum optomechanics experiments at room temperature, *Phys. Rev. Lett.* **116**, 147202 (2016).
- [19] M. Abdi, M.-J. Hwang, M. Aghtar, and M. B. Plenio, Spin-mechanical scheme with color centers in hexagonal boron nitride membranes, *Phys. Rev. Lett.* **119**, 233602 (2017).
- [20] K. V. Keesidis, S. D. Bennett, S. Portolan, M. D. Lukin, and P. Rabl, Phonon cooling and lasing with nitrogen-vacancy centers in diamond, *Phys. Rev. B* **88**, 064105 (2013).
- [21] E. R. MacQuarrie, M. Otten, S. K. Gray, and G. D. Fuchs, Cooling a mechanical resonator with nitrogen-vacancy centres using a room temperature excited state spin-strain interaction, *Nat. Commun.* **8**, 14358 (2017).
- [22] C. L. Cortes, M. Otten, and S. K. Gray, Ground-state cooling enabled by critical coupling and dark entangled states, *Phys. Rev. B* **99**, 014107 (2019).
- [23] Y.-D. Wang, Y. Li, F. Xue, C. Bruder, and K. Semba, Cooling a micromechanical resonator by quantum back-action from a noisy qubit, *Phys. Rev. B* **80**, 144508 (2009).
- [24] Y. Li, L.-A. Wu, Y.-D. Wang, and L.-P. Yang, Nondeterministic ultrafast ground-state cooling of a mechanical resonator, *Phys. Rev. B* **84**, 094502 (2011).
- [25] P. Zhang, Y. D. Wang, and C. P. Sun, Cooling mechanism for a nanomechanical resonator by periodic coupling to a Cooper pair box, *Phys. Rev. Lett.* **95**, 097204 (2005).
- [26] B.-y. Zhou and G.-x. Li, Ground-state cooling of a nanomechanical resonator via single-polariton optomechanics in a coupled quantum-dot-cavity system, *Phys. Rev. A* **94**, 033809 (2016).
- [27] I. Wilson-Rae, P. Zoller, and A. Imamoglu, Laser cooling of a nanomechanical resonator mode to its quantum ground state, *Phys. Rev. Lett.* **92**, 075507 (2004).
- [28] P. Rabl, Cooling of mechanical motion with a two-level system: The high-temperature regime, *Phys. Rev. B* **82**, 165320 (2010).
- [29] J.-p. Zhu and G.-x. Li, Ground-state cooling of a mechanical resonator by single- and two-phonon processes, *J. Appl. Phys.* **111**, 033704 (2012).
- [30] F. Elste, S. M. Girvin, and A. A. Clerk, Quantum noise interference and backaction cooling in cavity nanomechanics, *Phys. Rev. Lett.* **102**, 207209 (2009).
- [31] J. Chan, T. Alegre, A. H. Safavi-Naeini, J. T. Hill, A. Krause, S. Gröblacher, M. Aspelmeyer, and O. Painter, Laser cooling of a nanomechanical oscillator into its quantum ground state, *Nature (London)* **478**, 89 (2011).
- [32] Y.-C. Liu, Y.-F. Xiao, X. Luan, Q. Gong, and C. W. Wong, Coupled cavities for motional ground-state cooling and strong optomechanical coupling, *Phys. Rev. A* **91**, 033818 (2015).
- [33] Q. Mu, C. Lang, and P. Lin, Dynamic cooling of a micromechanical membrane in a double-cavity optomechanical system, *Int. J. Theor. Phys.* **59**, 454 (2020).
- [34] Y.-L. Liu and Y.-x. Liu, Energy-localization-enhanced ground-state cooling of a mechanical resonator from room temperature in optomechanics using a gain cavity, *Phys. Rev. A* **96**, 023812 (2017).
- [35] Y. Guo, K. Li, W. Nie, and Y. Li, Electromagnetically-induced-transparency-like ground-state cooling in a double-cavity optomechanical system, *Phys. Rev. A* **90**, 053841 (2014).
- [36] J. Kim, S. Song, Y.-H. Kim, and S. K. Park, Recent progress of quantum dot-based photonic devices and systems: A comprehensive review of materials, devices, and applications, *Small Struct.* **2**, 2000024 (2021).
- [37] S. G. Carter, A. S. Bracker, M. K. Yakes, M. K. Zalalutdinov, M. Kim, C. S. Kim, B. Lee, and D. Gammon, Tunable coupling of a double quantum dot spin system to a mechanical resonator, *Nano Lett.* **19**, 6166 (2019).
- [38] M. Montinaro, G. Wüst, M. Munsch, Y. Fontana, E. Russo-Averchi, M. Heiss, A. Fontcuberta I Morral, R. J. Warburton, and M. Poggio, Quantum dot opto-mechanics in a fully self-assembled nanowire, *Nano Lett.* **14**, 4454 (2014).
- [39] M. Khosla, S. Rao, and S. Gupta, Polarons explain luminescence behavior of colloidal quantum dots at low temperature, *Sci. Rep.* **8**, 8385 (2018).
- [40] J. Restrepo, C. Ciuti, and I. Favero, Single-polariton optomechanics, *Phys. Rev. Lett.* **112**, 013601 (2014).
- [41] K. Müller, K. A. Fischer, A. Rundquist, C. Dory, K. G. Lagoudakis, T. Sarmiento, Y. A. Kelaita, V. Borish, and J. Vučković, Ultrafast polariton-phonon dynamics of strongly coupled quantum dot-nanocavity systems, *Phys. Rev. X* **5**, 031006 (2015).
- [42] L. Biadala, Y. Louyer, P. Tamarat, and B. Lounis, Direct observation of the two lowest exciton zero-phonon lines in single CdSe/ZnS nanocrystals, *Phys. Rev. Lett.* **103**, 037404 (2009).
- [43] J. Johansson, P. Nation, and F. Nori, QuTiP 2: A Python framework for the dynamics of open quantum systems, *Comput. Phys. Commun.* **184**, 1234 (2013).
- [44] C. Gautham, D. W. Snoke, A. Rastelli, and O. G. Schmidt, Time-resolved two-photon excitation of dark states in quantum dots, *Appl. Phys. Lett.* **104**, 143114 (2014).

- [45] Q. Lu, X. Chen, H. Yang, X. Wu, and S. Xie, Ultrahigh Purcell factor, improved sensitivity, and enhanced optical force in dielectric bowtie whispering-gallery-mode resonators, *IEEE Photonics J.* **9**, 4502210 (2017).
- [46] J. Y. Lee, X. Lu, and Q. Lin, High-Q silicon carbide photonic-crystal cavities, *Appl. Phys. Lett.* **106**, 041106 (2015).
- [47] B. Schumacher and M. Westmoreland, *Quantum Processes Systems, and Information* (Cambridge University Press, Cambridge, 2010).
- [48] B. R. Fisher, H.-J. Eisler, N. E. Stott, and M. G. Bawendi, Emission intensity dependence and single-exponential behavior in single colloidal quantum dot fluorescence lifetimes, *J. Phys. Chem. B* **108**, 143 (2004).
- [49] I. S. Nikolaev, P. Lodahl, A. F. van Driel, A. F. Koenderink, and W. L. Vos, Strongly nonexponential time-resolved fluorescence of quantum-dot ensembles in three-dimensional photonic crystals, *Phys. Rev. B* **75**, 115302 (2007).
- [50] T. Neuman and J. Aizpurua, Origin of the asymmetric light emission from molecular exciton-polaritons, *Optica* **5**, 1247 (2018).
- [51] D. T. Nguyen, C. Baker, W. Hease, S. Sevil, P. Senellart, A. Lemaître, S. Ducci, G. Leo, and I. Favero, Ultra-high Q-frequency product for optomechanical disk resonators with a mechanical shield, *Appl. Phys. Lett.* **103**, 241112 (2013).
- [52] B. Guha, F. Marsault, F. Cadiz, L. Morgenroth, V. Ulin, V. Berkovitz, A. Lemaître, C. Gomez, A. Amo, S. Combrié *et al.*, Surface-enhanced gallium arsenide photonic resonator with quality factor of  $6 \times 10^6$ , *Optica* **4**, 218 (2017).
- [53] C. Baker, W. Hease, D.-T. Nguyen, A. Andronico, S. Ducci, G. Leo, and I. Favero, Photoelastic coupling in gallium arsenide optomechanical disk resonators, *Opt. Express* **22**, 14072 (2014).
- [54] J. P. Reithmaier, Strong exciton-photon coupling in semiconductor quantum dot systems, *Semicond. Sci. Technol.* **23**, 123001 (2008).
- [55] E. Peter, P. Senellart, D. Martrou, A. Lemaître, J. Hours, J. M. Gérard, and J. Bloch, Exciton-photon strong-coupling regime for a single quantum dot embedded in a microcavity, *Phys. Rev. Lett.* **95**, 067401 (2005).
- [56] P. Lodahl, A. Floris van Driel, I. S. Nikolaev, A. Irman, K. Overgaag, D. Vanmaekelbergh, and W. L. Vos, Controlling the dynamics of spontaneous emission from quantum dots by photonic crystals, *Nature (London)* **430**, 654 (2004).
- [57] V. Giesz, N. Somaschi, G. Hornecker, T. Grange, B. Reznichenko, L. De Santis, J. Demory, C. Gomez, I. Sagnes, A. Lemaître *et al.*, Coherent manipulation of a solid-state artificial atom with few photons, *Nat. Commun.* **7**, 11986 (2016).
- [58] A. Laucht, N. Hauke, J. Villas-Bôas, F. Hofbauer, G. Böhm, M. Kaniber, and J. Finley, Dephasing of exciton polaritons in photoexcited InGaAs quantum dots in GaAs nanocavities, *Phys. Rev. Lett.* **103**, 087405 (2009).
- [59] A. Kudelski, A. Lemaître, A. Miard, P. Voisin, T. C. M. Graham, R. J. Warburton, and O. Krebs, Optically probing the fine structure of a single Mn atom in an InAs quantum dot, *Phys. Rev. Lett.* **99**, 247209 (2007).
- [60] O. Krebs, E. Benjamin, and A. Lemaître, Magnetic anisotropy of singly Mn-doped InAs/GaAs quantum dots, *Phys. Rev. B* **80**, 165315 (2009).
- [61] M. O. Scully and M. S. Zubairy, *Quantum Optics* (Cambridge University Press, Cambridge, 1999).
- [62] R. Dum, A. S. Parkins, P. Zoller, and C. W. Gardiner, Monte Carlo simulation of master equations in quantum optics for vacuum, thermal, and squeezed reservoirs, *Phys. Rev. A* **46**, 4382 (1992).
- [63] A. J. Daley, Quantum trajectories and open many-body quantum systems, *Adv. Phys.* **63**, 77 (2014).
- [64] D. Manzano, A short introduction to the Lindblad master equation, *AIP Adv.* **10**, 025106 (2020).
- [65] J. Restrepo, I. Favero, and C. Ciuti, Fully coupled hybrid cavity optomechanics: Quantum interferences and correlations, *Phys. Rev. A* **95**, 023832 (2017).